Facultad de Ciencias

Estudio de modelos simplificados de materia oscura usando el programa MasterCode

(Study of simplified dark matter models using the MasterCode framework)

Trabajo de Fin de Grado
para acceder al

GRADO EN FíSICA

Autor: Marta Bárcena Rodríguez

Director: Alicia Calderón Tazón

Co-Director: Sven Heinemeyer

Septiembre – 2021

Contents

Acknowledgements

First of all, I would like to thank Alicia Calderón, Sven Heinemeyer and Emanuele Bagnaschi for all the support and guidance provided throughout this work. I have learned a lot, not just about particle physics but also about what it means to do real research, which I especially appreciate. Thank you for the time spent on this work, the helpful discussions and your advice. I also wanted to thank Edwin Goh Duo Yao for generating the first set of points and the MasterCode Collaboration for allowing me to use the code.

Thanks to my family for being a support all these years. Last but not least, thanks to all my friends in physics and mathematics, both in Santander and Manchester, for all the moments we have spent together.

Abstract

In the present work, we perform a global analysis of a dark matter simplified model (DMSM) with a leptophilic spin-1 vector mediator that interacts with the Standard Model (SM) particles and connects them to the dark matter (DM) particles. The five parameters that characterise our model are the mass of the mediator (m_Y), the mass of the DM particle (m_{DM}) and the mediator couplings to the DM particles (g_{DM}), to leptons (g_l) and quarks (g_q). In addition, we include some of the most recent experimental results as constraints on our model. In particular, we implement the most relevant results from the LHC experiments (from monojet, dijet and dilepton searches) and direct detection constraints (LUX, PandaX and XENON experiments). We also require our model to give the correct value for the DM relic density, in agreement with the cosmological observations from the Planck experiments on measuring the cosmic microwave background (CMB) anisotropies. The main tool used for this work is `MasterCode`, which is a framework that performs global analyses on multidimensional parameter spaces. Given our model, `MasterCode` computes the physics observables in all the parameter space and determines how well the model fits the experimental observations. We analyse the results on various planes of the parameter space, outlying which regions are excluded by the previous experiments and which ones are still a physical option.

Keywords: dark matter, dark matter simplified models, MasterCode, dark matter relic density, LHC.

Resumen

En este trabajo realizamos un análisis global de un modelo simplificado de materia oscura (DMSM) con un mediador vectorial leptofílico de spin-1 que interactúa con las partículas del Modelo Estándar (SM) y las conecta con las partículas de materia oscura (DM). Los cinco parámetros que caracterizan nuestro modelo son la masa del mediador (m_Y), la masa de la partícula de materia oscura (m_{DM}) y los acoplamientos del mediador a las partículas de materia oscura (g_{DM}), a los leptones (g_l) y a los quarks (g_q). Además, incluimos algunos de los resultados experimentales más recientes como restricciones de nuestro modelo. En particular, implementamos los resultados más relevantes de los experimentos del LHC (de las búsquedas de monojets, dijets y dileptones) y de experimentos de detección directa (experimentos LUX, PandaX y XENON). También requerimos que nuestro modelo dé el valor correcto para la densidad reliquia de materia oscura, de acuerdo con las observaciones cosmológicas del experimento Planck que mide las anisotropías del fondo cósmico de microondas (CMB). La principal herramienta utilizada para este trabajo es el programa `MasterCode`, que realiza el análisis global en un espacio de parámetros multidimensional y determina lo bien que nuestro modelo se ajusta a las observaciones experimentales. Analizamos los resultados en varios planos del espacio de parámetros, destacando qué regiones están excluidas por los experimentos anteriores y cuáles siguen siendo una opción física.

Palabras clave: materia oscura, modelos simplificados de búsqueda de materia oscura, MasterCode, densidad reliquia de materia oscura, LHC.

Chapter 1

Introduction

Everything we can see in the Universe is made of ordinary matter: the Earth, the Sun, the stars, etc. The Standard Model (SM) of particle physics describes the fundamental structure of such matter: the elementary particles and their interactions. Up to date, most of the SM theoretical predictions have been tested successfully. However, there are still some questions in particle physics left unanswered by the SM.

According to cosmological and astrophysical observations, ordinary matter only accounts for 5% of the composition of the Universe. Then, what is the rest of the Universe made of? Over the past decades, several experiments have tried to throw light on this topic and have found several pieces of evidence for the existence of a new type of matter that does not absorb or emit electromagnetic waves. Therefore, it is not visible to us, and this is why it is called dark matter (DM). But whether DM is made of elementary particles or compact objects, such as black holes, remains unknown. Finding an explanation about the nature of DM and its interactions with ordinary matter are undoubtedly two of the most crucial issues in modern physics. If we came up with the theory and the experimental results that entirely explain the physical nature of DM, it would help us better understand the composition of the Universe and how it holds together.

One of the many strategies we can take to study DM is to produce it in particle colliders such as the Large Hadron Collider (LHC) at the European Organization for Nuclear Research (CERN). Following this approach, we can build a simplified model for DM production at the LHC as our theoretical framework. The goal of this work is to perform a global fit of the free parameters of this model and include the most recent experimental results as constraints. These results come from different DM search experiments, such as LHC experiments (A Toroidal LHC ApparatuS [ATLAS] [1] and the Compact Muon Solenoid [CMS] [2]), direct detection experiments (the Large Underground Xenon DM experiment [LUX] [3], the Particle and Astrophysical Xenon Detector [PandaX] [4] and the XENON experiment [XENO1T]) [5]) and cosmological observations (Planck measurements of the cosmic microwave background (CMB) anisotropies [6]). The results of this global fit will help identify which regions of our model's parameter space are compatible with the observations and which ones are excluded. They will also allow us to determine which parameter space is still accessible at the LHC and define a search strategy for future LHC data acquisition. Finally, they could help develop future experiments that could focus on the still allowed regions of the parameter space.

This work is organised as follows. In this chapter, we first present a brief review of the experimental evidence for the existence of DM and of the most promising candidate to explain it: the Weakly Interacting Massive Particles. We then describe the WIMP model focusing on the concept of DM relic density. We finish chapter 1 with the three DM detection approaches: direct detection, indirect detection and production at colliders. In chapter 2, we briefly review the Standard Model of particle physics. Then, we discuss the simplified model used in this work as the theoretical framework for studying DM production at the LHC and its interactions with SM particles. We also give all the details about the five parameters that characterise such model. The experimental constraints are described in chapter 3: the DM relic density constraint, direct DM searches constraints and LHC constraints. In chapter 4, we review all the computational tools used throughout this work, with particular attention on `MasterCode`, which is the framework on which it is based. We also give a more statistical perspective on the sampling process, and we finish this chapter with some comments about the profiling process. The analysis of the results is discussed in chapter 5, and the conclusions and future work perspectives in chapter 6.

1.1 Experimental evidences for dark matter

As said before, we cannot see DM, but we know it exists due to its gravitational interaction with visible objects that we can detect. One of the most clarifying hints that indicates the existence of DM are the results from the study of anisotropies in the CMB. The CMB, which is the leftover radiation produced in the early stages of the Universe, gives an estimation of the total DM mass density and other constituents of the Universe. Indeed, the latest results from the Planck experiments on measuring the CMB anisotropies have shown that 27% of the Universe is made of DM and 68% of dark energy[1] [6]. The remaining 5% is the already known ordinary matter. Another hint for the existence of DM is the galaxies' rotation velocity. The incompatibility between the measurements of these velocities and Newton's law of universal gravitation led to the conclusion that galaxies are surrounded by a DM halo far more massive than the galaxy itself [7]. Additionally, results from the observation of gravitational lensing show that the path of light is bent due to the DM mass. This phenomenon is observed from Earth through space telescopes like the Hubble Space Telescope (HST).

There is no experimental evidence that DM interacts with either the electromagnetic or the strong force, so the most widespread theory is that DM interacts with ordinary matter only through the weak force. The possibility that DM is made of elementary particles described by the SM has been rejected. In particular, neutrinos have been the most studied SM particles since they are neutral and interact weakly, which has led to the idea that they could be good candidates for DM particles. They are rejected because the structures formed by DM depend on its velocity, and the experimental results conclude that DM in the cosmos is cold[2]. Since neutrinos are highly relativistic, they would form hot DM, which contradicts such observations. Therefore, if we assume that DM particles exist, we need to develop a theory beyond the SM that accounts for these new particles. Focusing on the belief that DM particles interact through the weak force, the leading candidates are the so-called Weakly Interacting Massive Particles (WIMPs). WIMPs are supposed to be charge-neutral, colourless and have masses in the GeV-TeV range, which is around the weak scale.

The particles we observe today are relics from the early Universe, including possible DM particles. Indeed, the current DM abundance in the Universe remains constant and is called DM relic density. Various theoretical models based on WIMPs yield the correct value for this DM abundance. A very general model that describes how the relic density evolves over time and temperature is the freeze-out scenario shown in figure 1.1. According to this model, when the Universe was dense and hot, all the particles were in thermal equilibrium. During this time, the temperature was such that

---

[1] Dark energy is a form of energy which we know that exists and how much there is in the Universe. Nevertheless, everything else about dark energy remains unknown.

[2] DM is composed of hot DM, cold DM and warm DM. Hot DM particles are relativistic, so their kinetic energy is of the order of their rest mass or even higher. In contrast, cold DM particles are not relativistic, and warm DM particles are in a mid-point.

the annihilation of SM particle-antiparticle pairs had enough energy to produce pairs of WIMPs. Conversely, WIMPs could also annihilate and produce SM particle-antiparticle pairs so that the rates of production and annihilation of WIMPs were the same. Whilst the Universe expanded, the freeze-out happened: the decrease in temperature caused the SM particles not to have enough thermal energy to create heavier particles, and the production of WIMPs dropped. Then, the decay into lighter particles (DM DM $\longrightarrow$ SM SM) dominated over the decay into heavier particles (SM SM $\longrightarrow$ DM DM), resulting in an imbalance between the DM and SM particles density. Since there were fewer DM particles and more separation between them, the frequency of such processes also decreased. At some point, the density of DM particles reached a constant value as it was no longer affected by the interactions [8, 9]. The Boltzmann equation describes this process, and its solution is shown in figure 1.1. This quantity, $\Omega_{\text{DM}}h^2$, is what we call the DM thermal relic density, and it is measurable experimentally. From the latest results of the Planck experiment, we know with high accuracy the current value of the total DM relic density:

$$\Omega_{\text{DM}}h^2 = 0.118 \pm 0.001 \tag{1.1}$$

with $h = H_0/(100\text{km}/(\text{sMpc}))$, where H_0 is the Hubble constant ($H_0 = 2.176 \cdot 10^{-18}\text{s}^{-1}$) and represents the current rate of expansion of the Universe [6].

According to this model, the following equation shows the relationship between the relic density and the WIMP annihilation cross-section σ_{ann} (i.e. the probability that such interaction takes place):

$$\Omega_{\text{DM}}h^2 = \frac{m_{\text{DM}}}{\rho_c}\frac{H_0}{\langle\sigma_{\text{ann}}v\rangle}h^2 \tag{1.2}$$

where ρ_c denotes the density of matter that the Universe needs to be flat, and v is the relative velocity of the WIMP [10]. Therefore, if we take the observed value of $\Omega_{\text{DM}}h^2$ (eq. 1.1) and m_{DM} in the GeV-TeV range and compute the annihilation cross-section σ_{ann} according to equation 1.2, we get a value which is in the range of the weak interaction cross-section. Thus, the fact that DM particles in the WIMP model (mass in the weak range and weak scale cross-sections with visible matter) reproduce the observed DM relic density is the so-called "WIMP Miracle" and is the reason for the widespread acceptance of this model. Furthermore, if DM particles have masses in such range, they could be produced at the LHC given its available centre-of-mass energy.

Note that in figure 1.1, we use χ to refer to the DM particle. More details on this are given in the following chapter. Throughout this work, we mainly use $\Omega_\chi h^2$ to refer to the DM relic density, which is equivalent to $\Omega_{\text{DM}}h^2$.

1.2 Searches for dark matter

We could take three approaches on the search for DM: direct detection, indirect detection, and production at colliders. Figure 1.2 shows a schematic representation of these three DM detection channels. First, assuming that the galaxy's halo is full of WIMPs, direct detection experiments pretend to observe the scattering between WIMPs coming from our galaxy and atomic nuclei in Earth-based detectors (upward direction in the figure). When the interaction occurs, the WIMP transfers a certain amount of momentum to the nuclei, which experiences a recoil that can be detected. To minimise background signals coming from cosmic rays or radioactivity that could interfere when measuring the recoil, the detectors in these experiments are placed underground. For example, this is what the Dark Matter in CCDs (DAMIC) experiment does at the SNOLAB underground laboratory in Canada [12]. Other direct detection experiments based on DM particles scattering of xenon atoms in underground detectors are the LUX experiment in the USA, the XENON experiment in Italy, and the PandaX experiment in China [3–5]. On the other hand, indirect

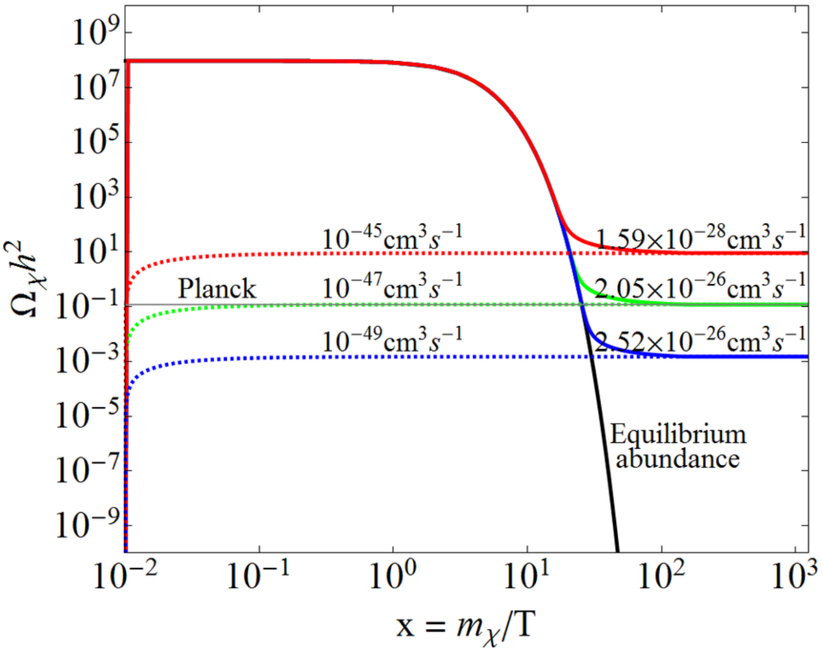

Figure 1.1: Evolution of the relic density $\Omega_\chi h^2$ as a function of m_χ/T for a WIMP of mass m_χ in the early Universe, where χ denotes the WIMP particle and T the temperature. The horizontal line represents the observed value of the relic density. The black line represents the case where the production would drop to zero if the Universe were not expanding. The red and blue lines correspond to the uncertainty bands of the annihilation cross-sections [11].

detection experiments analyse the products of the DM annihilation in the galaxies' halo. Whereas for direct detection the DM particles scatter with SM particles, for indirect detection pairs of DM particles collide and annihilate into SM particles (rightward direction). The aim is to infer the features of the DM annihilation from the study of the interaction products, such as neutrinos coming from the Sun or photons from the halos. Finally, according to the WIMP model and given the range of masses that it predicts, particle accelerators like the Large Hadron Collider (LHC) seem to be a potential place to produce such DM particles. The production of DM particles at a particle accelerator consists of two SM particles interacting at high energies and producing pairs of DM particles (leftward direction). For the time being, no signal of DM particles has been detected by any experiment.

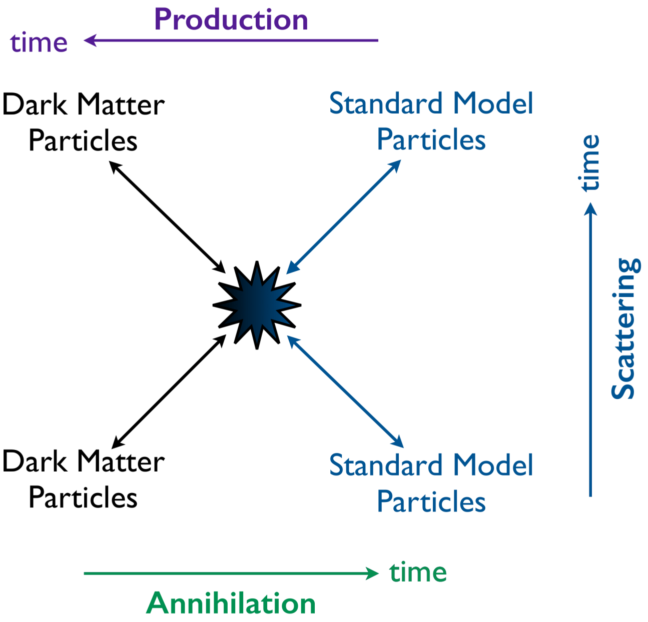

Figure 1.2: Scheme of the three DM detection approaches: annihilation (indirect detection), scattering (direct detection) and production at colliders [13].

Chapter 2

Dark matter simplified models and parameters

On the theoretical framework, the key point in the search for DM is to understand the mechanisms and processes that bring DM into thermal and kinetic equilibrium. To do so, we could build different models to interpret the experimental results. In this work, we are interested in describing the production of DM at the LHC, for which we take a very general approach: the simplified models for DM searches. Involving a few free parameters, Dark Matter Simplified Models (DMSM) give an accurate kinematic description of the DM production and its interactions with the SM particles at the LHC. We require these models to be complete enough in order to account for the physical processes of DM production at the LHC, but without the complexity of a full theory. In particular, the model used in this work is characterised by five parameters: the mass of the mediator (m_Y), the mass of the DM particle (m_{DM}) and the mediator couplings to the DM particles (g_{DM}), to leptons (g_l) and quarks (g_q). The discussion of these concepts is given later in this chapter, but for now, the parametrisation is schematised in figure 2.1[3].

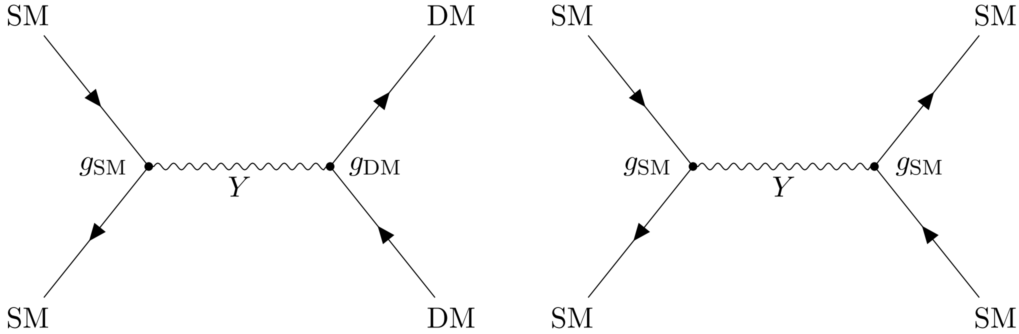

Figure 2.1: Feynman diagrams for the interaction of two SM particles in the initial state, the mediator Y, and the production of a pair of DM (left) or SM particles (right) in the final state. The parameters of our model are the mass of the mediator (m_Y), the mass of the DM particle (m_{DM}), the mediator couplings to the DM particles (g_{DM}) and to the SM particles (g_{SM}) which can be leptons (g_l) or quarks (g_q). The time direction is from left to right. The initial state particles are on the left, and the final state ones are on the right.

---

[3] All the Feynman diagrams shown in this work have been produced with the LaTeX package TikZ-Feynman [14].

2.1 Underlying concepts

Taking a step back to the SM, we recall that the two basic constituents of ordinary matter are fermions and bosons, as summarized in figure 2.2. On the one hand, fermions are half-integer spin particles, can be either leptons (e, μ, τ, ν_e, ν_μ, ν_τ) or quarks (u, d, c, s, t, b), and they are classified into three generations depending on their masses. Bosons, on the other hand, are integer spin particles. This group includes the Higgs boson, responsible for the mass of the fundamental particles, and the four gauge bosons, which are the carriers of the fundamental forces between particles (gravity, electromagnetism, weak force and strong force). Gauge bosons are also called mediator particles because they act like the propagators of the interactions, as shown in figure 2.1, where the initial state particles (SM) annihilate and form an intermediate mediator particle (Y) that subsequently decays to the final state particles (DM or SM). Regarding DM, we assume that it is composed of a single particle: a neutral Dirac fermion χ, which is a spin-1/2 particle that is different from its antiparticle[4]. This assumption and the parameters used throughout this work follow the recommendations of the LHC Dark Matter Working Group (LHCDMWG) [15–17]. Indeed, two of the parameters of our model are the mass of the mediator (m_Y) and the mass of the DM particle (we can write m_χ or m_{DM}, indistinctly).

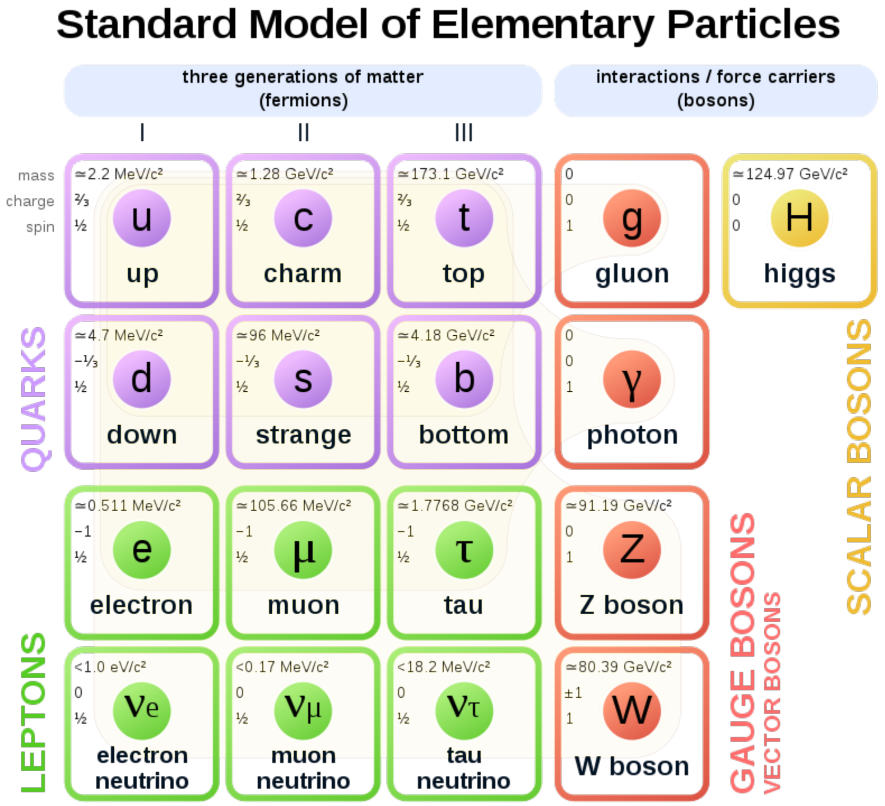

Figure 2.2: Particles of the Standard Model of particle physics. [18]

In chapter 1, we discussed the study of DM from its interactions with SM particles at the LHC. For this purpose, we define a simplified model which includes a spin-1 mediator particle that interacts with the SM particles and connects them to the DM particles. The LHC is a proton-proton collider, so the initial particles in figure 2.1 are always quarks. Regarding the final states, the mediator can

---

[4] With this assumption, we are avoiding the imposition of supersymmetry (SUSY models). For future works, we could consider the opposite: a Majorana fermion, which is a fermion that is its own antiparticle.

couple to another pair of quarks or to a pair of DM particles. However, we go further in this work by assuming a leptophilic model, which means that we allow the mediator to couple to leptons, so we can also find a pair of leptons in the final state. The strength of the interaction is what we denote coupling, g, and it is a dimensionless constant at each vertex. The couplings of the mediator to the DM particles (g_χ or g_{DM}), quarks (g_q) and leptons (g_l) are the other three parameters of our model.

Given a quantum state denoted $\psi(\vec{x},t)$, the parity transformation implies a change in the sign of the spatial coordinates. Depending on whether the interaction changes under this parity transformation, it is classified into scalar, pseudoscalar, vector or axial-vector. The operator associated with parity is the gamma matrix[5] γ^0, so that $\hat{P}\psi(\vec{x},t) = \gamma^0\psi(\vec{x},t) = \psi(-\vec{x},t)$. For instance, the temperature T is invariant under the action of the parity operator, and it is what we call a scalar. Other quantities like the momentum $\vec{p}$ are not invariant because the spatial coordinates are reversed under parity, thus they are called vector quantities. Axial-vectors or pseudovectors arise from the cross product of two vector quantities, therefore the spatial coordinates' sign is unchanged. For example, the angular momentum $L = \vec{x} \times \vec{p}$ is an axial-vector. Finally, pseudoscalars are taken from the product of a vector and an axial-vector, hence they change sign under parity transformations. For instance, the magnetic flux $\Phi = \vec{B} \cdot \vec{S}$ [19]. According to this classification, in such a simplified model, we can choose the type of interaction that takes place. We mainly talk about vector and axial-vector interactions throughout this work, so we use the superscripts V and A, respectively.

Lagrangians describe the interactions between particles in a mathematical sense. Considering the exchange of a spin-1 boson mediator, there are two types of interactions at each vertex: vector ($\bar{\phi_1}\gamma^\mu g^V\phi_2$) and axial-vector ($\bar{\phi_1}\gamma^\mu\gamma^5 g^A\phi_2$) [6]. Experimentally, it is observed that the weak interaction does not conserve parity. To account for this, the form of the weak interaction must be a linear combination of vector and axial-vector (V-A structure): ($\bar{\phi_1}\gamma^\mu(g^V - g^A\gamma^5)\phi_2$). Furthermore, we can describe the interaction by separating the vector and axial-vector components of the Lagrangian. For instance, considering the model of the vector coupling, g^V, between a general mediator Y and the DM particle as a Dirac fermion χ, the Lagrangian is as follows:

$$\mathcal{L} \supset -\bar{\chi}g_\chi^V\gamma^\mu\chi Y. \tag{2.1}$$

that for the interaction with quarks q is:

$$\mathcal{L} \supset -\sum_{i=u,d,b,t,c,s}\bar{q}_i g_{q_i}^V\gamma^\mu q_i Y. \tag{2.2}$$

and for the interaction with leptons l:

$$\mathcal{L} \supset -\sum_{i=e,\mu,\tau,\nu_e,\nu_\mu,\nu_\tau}\bar{l}_i g_{l_i}^V\gamma^\mu l_i Y. \tag{2.3}$$

with q and l denoting the spinors associated with quarks and leptons, Y is the mediator and g^V the vector coupling between the mediator and the DM particles, quarks or leptons, respectively. It should be noted that the sum extends over all quarks and leptons.

Another important concept we need to take into consideration is the decay width of the mediator, Γ_Y, which is proportional to the inverse of its lifetime, $\Gamma_Y = \frac{1}{\tau}$. It can be thought of as a parameter

---

[5] The gamma matrices or Dirac matrices (γ^i) are related to the Pauli matrices (σ_i):
$\sigma_1 = \begin{pmatrix} 0 & 1 \\ 1 & 0 \end{pmatrix}$, $\sigma_2 = \begin{pmatrix} 0 & -i \\ i & 0 \end{pmatrix}$, $\sigma_3 = \begin{pmatrix} 1 & 0 \\ 0 & -1 \end{pmatrix}$; $\gamma^0 = \begin{pmatrix} I & 0 \\ 0 & -I \end{pmatrix}$, $\gamma^i = \begin{pmatrix} 0 & \sigma_i \\ -\sigma_i & 0 \end{pmatrix}$, $\gamma^5 = i\gamma^0\gamma^1\gamma^2\gamma^3$.

[6] ϕ_1 and ϕ_2 denote two general spinors (i.e. four-component wavefunctions) and γ is the gamma matrix. g^V and g^A are the couplings in a vector or axial-vector interaction, respectively.

representing the mediator's decay strength to the various decay modes. The following expressions give the total width of our vector mediator Y:

$$\Gamma_Y = \Gamma_Y^{\chi\bar{\chi}} + \sum_q \Gamma_Y^{q\bar{q}} + \sum_l \Gamma_Y^{ll}. \tag{2.4}$$

$$\Gamma_Y^{\chi\bar{\chi}} = \frac{g_\chi^2 m_Y}{12\pi}\left(1 + \frac{2m_\chi^2}{m_Y^2}\right)\sqrt{1 - \frac{4m_\chi^2}{m_Y^2}}. \tag{2.5}$$

$$\Gamma_Y^{q\bar{q}} = \frac{3g_q^2 m_Y}{12\pi}\left(1 + \frac{2m_q^2}{m_Y^2}\right)\sqrt{1 - \frac{4m_q^2}{m_Y^2}}. \tag{2.6}$$

$$\Gamma_Y^{l\bar{l}} = \frac{g_l^2 m_Y}{12\pi}\left(1 + \frac{2m_l^2}{m_Y^2}\right)\sqrt{1 - \frac{4m_l^2}{m_Y^2}}. \tag{2.7}$$

with $\Gamma_Y^{\chi\bar{\chi}}$, $\Gamma_Y^{q\bar{q}}$ and Γ_Y^{ll} denoting the partial widths of the mediator decaying to a pair of DM particles, a pair of quarks, and a pair of leptons respectively, m_q is the quark's mass and m_l the lepton's mass [16, 20]. Note that the sum extends over all quarks and leptons. It is important to remark that the three contributions are zero when $2m_i > m_Y$ such that $i = \chi, l, q$.

2.2 Dark matter simplified model with a leptophilic spin-1 vector mediator

To recap, taking the WIMP-like phenomenology as our basis, we require the DM production to be mediated by a neutral spin-1 mediator, Y, with a mass in the GeV - TeV range, so it is potentially possible to be produced at the LHC. A spin-1 mediator could be a vector or axial-vector particle, but we have chosen a vector mediator for this model, so all the couplings are vector couplings. Furthermore, this model is leptophilic, which means that it allows the interaction between the mediator and leptons. On the contrary, leptophobic models forbid such interactions (i.e. the coupling to leptons is always 0).

This work describes the simplified model defined by the following set of parameters:

$$\{m_Y, m_\chi, g_\chi^V, g_q^V, g_l^V\}$$

with m_Y denoting the mediator mass, m_χ the DM particle mass, and g_χ^V, g_q^V, g_l^V the vector couplings to DM, quarks and leptons, respectively. Note we are setting the axial part (g_χ^A, g_q^A, g_l^A) to zero, so we only consider a pure vector interaction. Besides, we assume that the interaction between the mediator and the SM particles is flavour-independent so that the mediator couples to all quarks and all leptons with the same strength. What is more, we take from the SM the lepton flavour universality, which means that we do not mix flavours. For example, the only way to annihilate an electron (e^-) is through its interaction with a positron (e^+). Hence, for this model, we could consider the coupling to (e^-, e^+), but not to (e^-, μ^+), and the same is considered for quarks.

The same study has been previously done considering the cases of both vector and axial-vector interactions with a spin-1 leptophobic mediator [21]. We take this work as our starting point to analyse the case for the vector interaction adding the coupling to leptons as a fifth parameter. For future studies, we could investigate our model for an axial-vector mediator.

Chapter 3

Experimental constraints

We have included some of the most relevant recent experimental results as constraints on our model. The aim is to use these results to see which regions of our parameter space are compatible with the observations and which ones are already excluded. In particular, we include the results from direct detection experiments, LHC searches and the value of the relic density shown in equation 1.1. All the details about the experiments and the constraints are detailed below. We have not considered any indirect detection experiments because they are insensitive for simplified models when $m_\chi > 50$ GeV, according to [22].

3.1 Dark matter relic density constraint

As explained in chapter 1, we know the current amount of DM density in the Universe with high precision (eq. 1.1). Therefore, we are interested in those combinations of the five parameters of our model for which the computed DM relic density reproduces the experimental value. The numerical computation of $\Omega_{\mathrm{DM}}h^2$ is done by `micrOMEGAs` [23]. More details on this program are given in chapter 4.

When using the relic abundance to set constraints on the parameters, we could take two different approaches. On the one hand, with the hypothesis of the WIMP model, we could assume that the DM particle χ is the only constituent responsible for generating this relic density, so that $\Omega_\chi h^2 \approx \Omega_{\mathrm{DM}}h^2$. On the other hand, we could impose the previous value as just an upper bound. In this way, we assume that if the relic density coming from the DM particles is less than the observed value, we still allow it because there could be something else contributing to the missing relic density.

Figure 3.1 shows the diagrams for the two processes in which DM annihilation can occur: annihilation through a mediator (left) and annihilation to pairs of mediators (right). The first one is called s-channel annihilation and was shown in the previous chapter: the process where the DM particles annihilate and form a mediator that decays to a pair of SM particles. The second one is the t-channel scattering, where the DM particles annihilate to a pair of mediators that subsequently decay to a pair of SM particles. It is important to remark that the s-channel (left) is kinematically accessible when $2m_\chi \geq m_Y$. The requirement for the t-channel annihilation (right) is $m_\chi \geq m_Y$. Since this model allows the mediator coupling to leptons, we also consider the corresponding diagrams with leptons (l) in the final states instead of quarks (q).

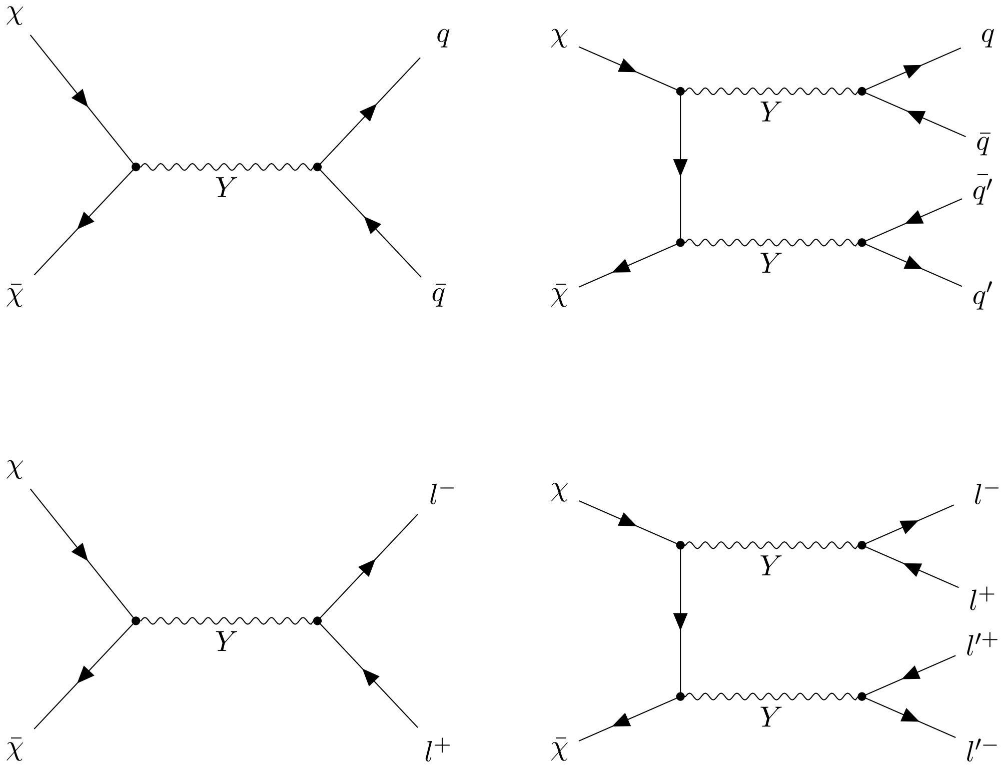

Figure 3.1: Feynman diagrams for the two processes contributing to DM annihilation: the annihilation through a single mediator in the s-channel (left) and the t-channel annihilation to a pair of mediators that subsequently decay to quarks or leptons (right). Y denotes a general mediator particle and χ ($\bar{\chi}$) the DM particles (antiparticles), while q and q' (l^- and l'^-) represent two general quarks (leptons), with $\bar{q}$ and $\bar{q}'$ (l^+ and l'^+) denoting their respective antiparticles.

As an introductory example, figure 3.2 compares the results for the relic density in the (m_Y, m_χ) plane for a spin-1 axial-vector mediator and different choices for the couplings. Figure 3.2a shows a leptophobic scenario with couplings $g_q^A = 0.25$, $g_\chi^A = 1.00$ and $g_l^A = 0.00$ and figure 3.2b a leptophilic scenario with couplings $g_q^A = 0.10$, $g_\chi^A = 1.00$ and $g_l^A = 0.10$. Both figures are coloured according to the values of $\Omega_\chi h^2$. We conclude that, for the previous values of the couplings and according to the colour bar, the DM relic density constraint excludes the dark blue regions because they give a higher value of $\Omega_\chi h^2$ than the observed one. Moreover, the shape of these areas depends on the choice of the couplings. For instance, we appreciate that the contour extends to slightly lower m_Y in the leptophilic scenario. The solid orange contours represent the points for which the computation of relic density gives exactly the right value: $\Omega_\chi h^2 = 0.118$, and the white regions where $\Omega_\chi h^2 < 0.118$. Additionally, figure 3.3 displays the same figures, but they are coloured according to the values of the likelihood $\Delta\chi^2 = \chi^2 - \chi^2_{\text{min}}$, where χ^2_{min} is the global minimum. Further comments on the likelihood of the model and its interpretation are given in the next chapter. For now, it is important to remark that each constraint defines a likelihood function, so we take the joint likelihood of all the experimental constraints that are taken into account. Such function is written as a χ^2 and depends on all the model parameters, in the sense that the lower the $\Delta\chi^2$, the better the point fits our model. Hence, the allowed regions (in white) are where the combination of the fixed couplings and masses satisfies all the constraints. In particular, they would give a value for the relic density that comes the closest to the measured one. In contrast, the dark regions do not satisfy one or more of the constraints. If we compare both figures, we observe that the points that have the lowest $\Delta\chi^2$ in figure 3.3 are those that reproduce the contours in 3.2, as we would expect. Comparing the results for the leptophobic and leptophilic scenarios, we observe that the diagonal $m_Y = 2m_\chi$ gives very small values of $\Delta\chi^2$ in both cases, and the orange contour above the diagonal extends towards lower values of m_Y in the leptophilic scenario. Since $g_\chi = 1$ in both scenarios, we can conclude that the distinct features in the results are a consequence of g_q and g_l.

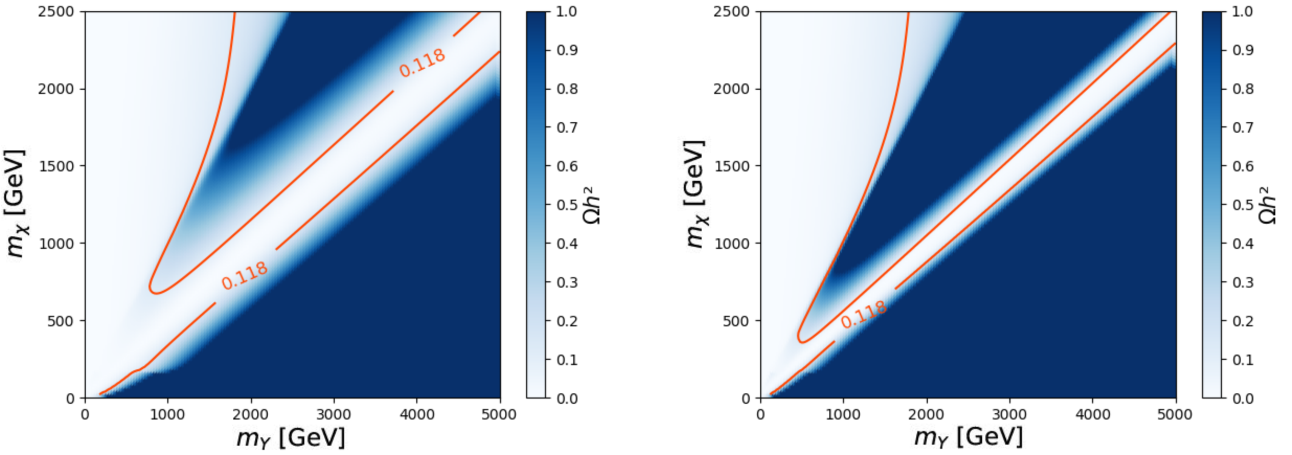

(a) Leptophobic: $g_q = 0.25$, $g_l = 0.00$ and $g_\chi = 1.00$. (b) Leptophilic : $g_q = g_l = 0.10$ and $g_\chi = 1.00$.

Figure 3.2: Representation of the relic density Ωh^2 in the (m_Y, m_χ) plane for a spin-1 axial-vector mediator. The figure compares two scenarios: leptophobic with couplings $g_q = 0.25$, $g_l = 0.00$ and $g_\chi = 1.00$ (left) and leptophilic with couplings $g_q = g_l = 0.10$ and $g_\chi = 1.00$ (right). The contour lines represent the regions of the parameter space where the combination of the masses and couplings give the exact observed value for the relic density: $\Omega h^2 = 0.118$. Both figures are coloured according to the values of Ωh^2.

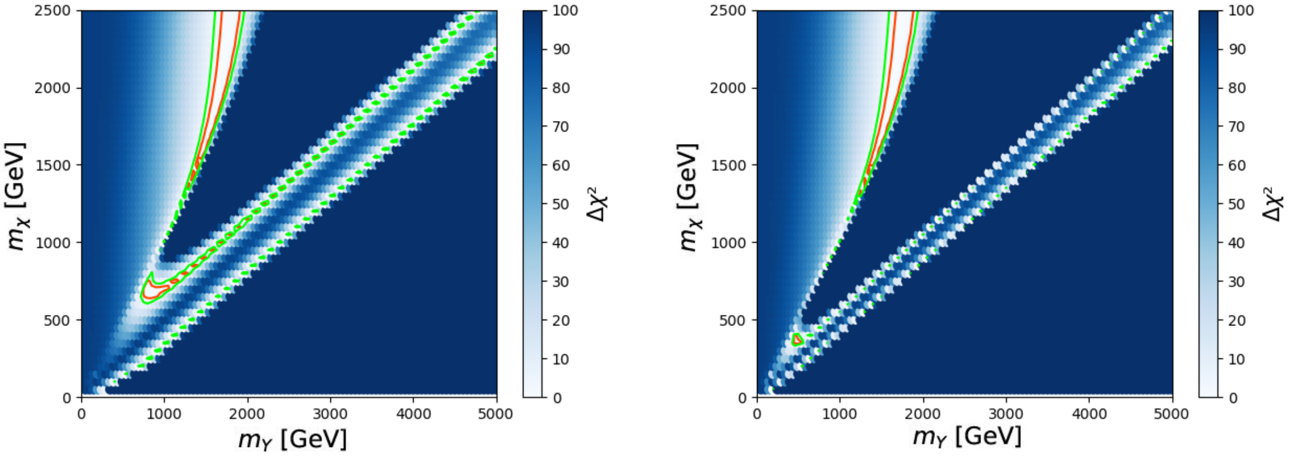

(a) Leptophobic: $g_q = 0.25$, $g_l = 0.00$ and $g_\chi = 1.00$. (b) Leptophilic : $g_q = g_l = 0.10$ and $g_\chi = 1.00$.

Figure 3.3: Representation of the likelihood function in the (m_Y, m_χ) plane for a spin-1 axial-vector mediator. The figure compares two scenarios: leptophobic with couplings $g_q = 0.25$, $g_l = 0.00$ and $g_\chi = 1.00$ (left) and leptophilic with couplings $g_q = g_l = 0.10$ and $g_\chi = 1.00$ (right). The contour lines represent the 1-σ (orange) and 2-σ (green) contours, which are the boundaries of the regions with $\Delta\chi^2 < 2.30$ and $\Delta\chi^2 < 5.99$, respectively. Both figures are coloured according to the values of $\Delta\chi^2 = \chi^2 - \chi^2_{\text{min}}$.

3.2 Direct DM searches constraints

As said before, direct detection experiments intend to discover DM particles from the products of their interaction with atomic nuclei. We make use of the most recent results from direct detection experiments such as LUX, PandaX and XENON1T to derive limits on the DM-nuclei scattering rate [24–26]. The three of them study the scattering between WIMPs and liquid xenon atoms through the nuclear recoils experienced by the latter. The numerical computation of the direct detection scattering cross-sections is done by `micrOMEGAs` [23]. More details on this program are given in chapter 4.

3.3 LHC constraints

The LHC, at CERN in Geneva, is the world's most powerful particle accelerator. It is located in a 27 km underground tunnel, and it accelerates particles up to a maximum energy of 14 TeV, with a speed close to the one of light. We have included several results from the two general-purpose LHC experiments: ATLAS and CMS. Both are designed to study very different particle physics processes, such as the Higgs boson, predictions on the SM, and even searches for new physics beyond the SM. In particular, we have taken the latest results from these experiments using data at a centre of mass energy of 13 TeV, collected during the Run 2 period (2015-2018) [27–34].

In this simplified model, the main production diagram at the LHC is the annihilation of two quarks. As seen in figure 3.4, we consider the processes in which the DM particles couple to quarks through a mediator that subsequently decays to a pair of WIMPs (top left) or to a pair of SM particles that can be either neutrinos (top right), quarks (bottom left) or leptons (bottom right). We now discuss two classes of signatures, which are the most important for the phenomenology of our model: mono-X searches (undetectable final states) and mediator searches (visible final states) [35].

- Mono-X searches. The final states are undetectable, so we try to infer their production from the other products of the interaction. WIMPs are only weakly interacting, and they are considered stable particles at least over the age of the Universe because, otherwise, there would be no relic density. Hence, if the mediator decays into two WIMPs, they escape the LHC detectors without leaving any visible track, but generating a momentum imbalance as a sign of their passage. If we analysed the interaction products and imposed momentum conservation, the momentum imbalance (called missing transverse energy) would be associated with the DM particles that have escaped. To detect this kind of process, we need to detect a signal that indicates that such an interaction has occurred. For this reason, we require the initial state to radiate particles that we can detect, such as photons, quarks or gluons. In this work, we focus on monojet signatures. For instance, in figure 3.4 top left, a pair of DM particles couple to quarks through a mediator that subsequently decays to a pair of DM particles. The initial quarks radiate a gluon and, since a free gluon cannot exist, it hadronizes generating a jet[7]. In the detector, we would find missing transverse energy recoiling against these visible energetic particles. As seen in figure 3.4 top right, we also include in the monojet search the same process with the mediator decaying to a pair of neutrinos that are also undetectable.

- Mediator searches. We consider the processes in which the mediator decays back to a pair of SM particles (quarks or leptons) that are visible in the detector, as seen in figure 3.4 bottom. The mediator decays immediately, so we cannot detect it, but we can trace back its properties from the final states, which leave visible tracks in the detectors. We consider experimental results

---

[7] A jet is a collimated bunch of particles produced after the hadronisation process of the radiated gluon. The hadronisation process forms hadrons (subatomic particles made of quarks) out of quarks and gluons (boson particle carrier of the strong nuclear force).

from the dijet (bottom left) and the dilepton (bottom right) final states analysis, in which the mediator decays to a pair of quarks or leptons, respectively. For the dilepton diagrams, we only consider charged leptons, as the experiments we take into account are not performed searching for neutrinos. What is more, they only take into account electrons and muons because ditau signatures are more difficult to identify cleanly [34].

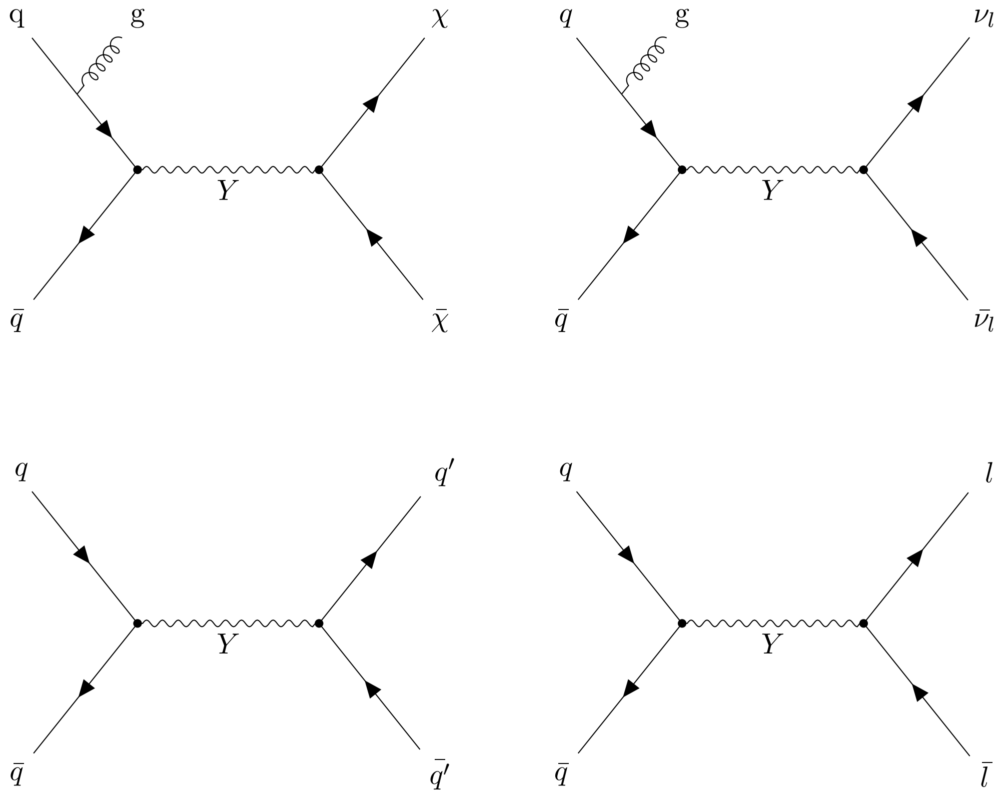

Figure 3.4: Feynman diagrams for a monojet (top), dijet (bottom left) and dilepton (bottom right) signatures. In these interactions, DM particles couple to quarks through a mediator that subsequently decays to either a pair of DM particles or neutrinos (monojet), to a pair of quarks (dijet) or a pair of leptons (dilepton). Y is the mediator particle, g the radiated gluon, χ ($\bar{\chi}$) the DM particles (antiparticles) and ν_l ($\bar{\nu_l}$) the neutrinos (antineutrinos) while q and q' (l^-) represent two general quarks (lepton), with $\bar{q}$ and $\bar{q'}$ (l^+) denoting their respective antiparticles. Note that the initial state quarks in the monojet diagrams radiate a gluon.

It is important to note that the decay of the mediator into a pair of DM particles is kinematically allowed only if $m_Y \geq 2m_\chi$. Otherwise, DM production is forbidden, and we can only consider the dijet and dilepton diagrams.

Chapter 4

Framework

As already mentioned, the main aim of this work is to perform a global study of our model, using constraints coming from different types of experiments, in order to find the still allowed parameter space regions. The main tool used for this purpose is the `MasterCode` program, which is a framework that performs multidimensional global analyses of Beyond the Standard Model Theories (BSM), focusing on SUSY and DMSM [21, 36, 37]. Given a specific model, `MasterCode` computes the physics observables in all the parameter space points and determines how well the model fits the experimental results.

`MasterCode` is a software framework that allows the user to run all the necessary softwares to study a given model, interfacing them in a consistent way. Some of the most important ones are the following. `Fastlim` implements the collider constraints [38]. The final state observables and the mediator properties are computed using the `Madgraph` program [39], while the `micrOMEGAs` program does the numerical computation of the direct detection cross-sections, and the DM observables, such as the DM relic density [23]. To sample the parameter space and find the regions with the best χ^2, `MasterCode` uses the `MultiNest` algorithm [40]. Details on this algorithm are given in the following section.

`MasterCode` is a multi-language framework. The calculation of the likelihood and the implementation of the constraints is written in C++. This language was chosen to have a high-performance code since we must compute the likelihood for every sampled point. The interface, which makes the code accessible for the users, and the computation of the physics observables are written in Python since it allows more flexibility and is more user-friendly than other languages. Cython is used to connect the Python codes to the C++ codes. Additionally, as we sample the parameter space, we want to store and manage all the data for each point, for which we use `sql` databases[8] [41]. In this way, each point (i.e. each combination of the five parameters) is associated with a row, and each column is an observable. I have worked with Python, the bash shell script, and the VIM editor in Linux for the scripting [42]. The VIM editor has different features from other script editors I have worked with before, so I learnt how to use its functionalities. For instance, it does not allow the use of the computer mouse, and it requires to master some key combinations, without which it is not possible to work efficiently. Regarding the visualisations, most of the plots shown in this work have been generated with existing scripts inside `MasterCode`. However, I have needed to change them to add some new features, such as the axes, colours or the display of new variables that were not defined. For this reason, I learnt how to use the Matplotlib library, which is a Python library helpful to produce all kinds of visualisations [43].

---

[8] SQL (Structured Query Language) is a database language for storing, accessing and managing data sets.

Other tools that have been necessary to use the `MasterCode` framework are listed below. First, to use the `MasterCode` environment, it would have been ideal to install it locally on my computer, but due to its large size and to avoid running out of space, I used a virtual machine (VM). The VM includes everything needed to run different operating systems regardless of which one runs on the computer. In particular, I have used a VM image, through the Oracle VM VirtualBox software, that contains the `MasterCode` environment running in the Linux system, while my laptop's operating system is Windows [44]. Inside the VM, a `docker` container is used to run the `MasterCode` environment [45]. A container is a unit of software that allows the user to run an application, such as codes, libraries and other system tools. In this way, we have everything required to compile and run `MasterCode` without performing the installation. Second, the CERN organisation allows users to connect to their cluster of computers remotely via ssh connections[9]. Since some of the processes that `MasterCode` runs require large computational resources that my laptop could not handle, I used this service to launch some of them. Inside the cluster, since `docker` is not available, we have used a `singularity` container that works in the same way [46]. Finally, to run some instances of the sampling, we have used `HTCondor`.The sampling process requires high CPU usage, so we decided to use this batch system available for CERN users [47]. This system splits the code into multiple jobs running in parallel so that the time required to minimise the χ^2 over the entire parameter space is considerably reduced.

4.1 Sampling and fitting

Likelihood functions are used to measure how well a statistical model fits a sample of data for given values of its parameters. In particular, since we want to find those values of the parameters that maximise the likelihood of our model, we use the chi-square statistic, χ^2. Thus, minimising the χ^2 is equivalent to maximising the likelihood since a low χ^2 means that the experimental data fit our model very well. Each constraint defines an individual likelihood function, so we need to compute the joint likelihood of all the experimental constraints that are taken into account. Inside `MasterCode` one can easily define a joint likelihood in terms of single constraints using a Python dictionary. The implementation of the constraints is done as follows. First, the likelihood functions are obtained from the parametrisation of the results of each experiment, formulated as a χ^2. Then, the joint likelihood function is computed as the sum of all the log-likelihood functions. Finally, this joint likelihood, written in terms of the model's parameters, is used to calculate the χ^2 value of each parameter space point. In the analysis of the results, we mainly use $\Delta\chi^2 = \chi^2 - \chi^2_{\text{min}}$ as a measure of the likelihood, where χ^2 represents the likelihood at a certain point and χ^2_{min} is the global minimum.

Parameter	Range
m_χ	(0, 2.5) TeV
m_Y	(0.1, 6) TeV
g_l	$(0, \sqrt{4\pi})$
g_q	$(0, \sqrt{4\pi})$
g_χ	$(0, \sqrt{4\pi})$

Table 4.1: Parameters of our model and regions where they are considered. Note that all the couplings are vector couplings.

---

[9] The ssh (or secure shell) connections allow remote access to a server via a secure channel in which all information is encrypted.

Next, we need to define the ranges in which each parameter is studied (table 4.1). Recall that we only consider a pure vector interaction for this work, which means that the three couplings are vector couplings. From now on, we drop the superscript V, and we refer to them as simply g. These limits are chosen to ensure that our parameter space is valid for the WIMPs' model and accessible at the LHC energy scale. A brief explanation of each range is given below. First, the weak interaction is mediated by the W and Z bosons, with masses $m_W = 80,4$ GeV/c^2 and $m_Z = 91,2$ GeV/c^2. Therefore, we take the lower limit of the mediator mass to be 100 GeV because these mass ranges are well studied, and there have been no signs of interaction with DM so far, so we can avoid this to focus on regions that are not extensively analysed. In addition, if the masses of Y and the Z are similar, we would enter the region where the Y and Z are mixed, and we should take additional constraints into account. On the other hand, nothing prevents us from going down to very low values of m_χ, so we take 0 Gev as the lower limit. We take 6 TeV and 2.5 TeV as the upper limits for m_Y and m_χ, respectively, so we avoid the regions where we would not have enough energy to produce the particles at the LHC, as the maximum reachable energy is 14 TeV. Second, all the couplings take 0 as the minimum value, as this would mean that these particles are not involved in the interaction, which is perfectly possible. The upper limit $\sqrt{4\pi}$ is imposed to ensure perturbativity in our calculations. Perturbation theory is often used in particle physics, and for our purpose, we have to ensure that the model remains perturbative so that all the calculations are adequate. If the strength of the interaction (i.e. the coupling) is small enough, we can effectively approximate it to a series expansion. If this value were over $\sqrt{4\pi}$, the series would not converge.

Now that the five parameters and the constraints that characterise the model are implemented, we can proceed to the sampling of the parameter space. In order to do so, we need to compute the observables and evaluate the χ^2 for a large number of points. Then, we find which regions are allowed and preferred by the data. This process needs many sample points to find the minimum values accurately, so it takes a huge amount of time. In order to work efficiently, we used the `MultiNest` algorithm as a minimisation procedure in computing the χ^2 in a multidimensional parameter space [37, 40]. The algorithm simulates some of the points in the parameter space with a nested sampling method. Since the parameter space is large, we segment it, so all the space is divided into a certain number of hypercubes to achieve more efficiency. Such hypercubes or boxes can be set to be logarithmic or linear. A logarithmic box means that the sample points are distributed uniformly on a logarithmic scale, i.e. small values of the parameters are sampled more frequently. As mentioned in the previous section, this process runs in `HTCondor`, launching multiple jobs running in parallel. `MultiNest` minimises the likelihood similarly to the gradient descent. Taking the slope that the likelihood function defines in the space, the idea is to follow the direction of the slope where the function decreases. When it cannot decrease anymore, the algorithm converges, and the minimum is reached. The last step is to merge all the databases. To make the process faster, only the points that satisfy $\chi^2 < 20$ are stored for performance.

For the analysis of the results, we generate the plots to see how the likelihood behaves if we project it onto the different planes of the parameter space. For every point in the 2-dimensional plane, we fix two of the parameters and minimise the χ^2 with respect to the remaining three. We call this procedure profiling, and it is done as follows. All the databases with the outcome from the samplings are stored in the EOS directory[10] of the project. From the points in the databases, I run the profile likelihood functions for a given set of planes. These planes are taken from the different combinations of pairs of the five parameters and other observables that are sometimes of interest, for instance, the relic density or the mediator widths. Then, the points with the lowest χ^2 are stored in a `ROOT` file[11]. In `MasterCode` the likelihood is recomputed every time a profiling is performed. Since computing

---

[10] EOS is the CERN's storage service

[11] `ROOT` is a data analysis framework used in high energy physics that allows the user to store, access and process vast amounts of data in a very fast way.

the χ^2 for each point is not particularly time-consuming, it is worthwhile to recalculate it to gain more flexibility in modifying the constraints. We do it this way because sometimes it is useful to change the values of a constraint, implement new ones, or see how the results vary if we remove one or the other. If we had to run the entire sampling every time such a modification is made, this work would take many months. Moreover, we only have to recompute the likelihood for those points that have been stored in the database during the sampling (i.e. those with $\chi^2 < 20$), so we do not really process that many points at this step. Afterwards, we profile the likelihood function taking as an input the previous database, the definition of the constraints sets (i.e. the total likelihood function) and the subspaces we want to display. The profilings are then transferred to the virtual machine, where `MasterCode` and the Matplotlib library have been used to generate the plots.

Sometimes it has been necessary to run more accurate samplings in smaller subspaces. As will be discussed in detail in the results, when the space is too large, we might have problems with the convergence of `MultiNest` in certain regions. To solve this, we run a sampling in a reduced parameter range. Then, we have to rerun the profiling with these new results. Inside `MasterCode`, we can join the outputs of several profilings. In this way, we can run the profiling on each sampling database and then merge them. This allows us to save a considerable amount of time compared to what we would need if we first merged the databases and then ran the profiling on this huge database.

Chapter 5

Results

This chapter presents the main results of this work. We recall our goal is to perform a global likelihood analysis on the search for DM particles at the LHC using the `MasterCode` framework. The theoretical model is a DM simplified model with a leptophilic spin-1 vector mediator, characterised by the following parameters:

$$\{m_Y, m_\chi, g_\chi, g_q, g_l\} \, .$$

The most recent results from DM searches (direct detection and LHC experiments) are included as constraints on the model, together with the imposition of the observed value for the relic density: $\Omega_{\mathrm{DM}}h^2 = 0.118 \pm 0.001$. After studying and interpreting the results, we conclude which regions of the parameter space are still allowed by the already published experimental results and which ones are forbidden.

5.1 General comments

Before proceeding with the analysis of the results, some considerations about the plots are given below. As an example, consider the (m_Y, m_χ) plane in figure 5.1. This plot displays $\Delta\chi^2$ coloured as a function of m_Y (x-axis) and m_χ (y-axis), which is obtained from the global fit results, where $\Delta\chi^2 = \chi^2 - \chi^2_{\mathrm{min}}$, and χ^2_{min} is the global minimum of the likelihood. First, it is important to emphasise that the points shown in the planes have two fixed parameters, which are the figure axes, and the remaining three are free parameters. Hence, for each fixed pair (m_Y, m_χ) in figure 5.1, we have different combinations for the values of the couplings, and each of them might give a different $\Delta\chi^2$. At each bin in the plot, we only show the point whose combination of the three free parameters gives the lowest $\Delta\chi^2$. Moreover, the displayed points are coloured according to the computed $\Delta\chi^2$, except for the grey and white points. The grey colour means that the points lie inside the consideration ranges (table 4.1), but their χ^2 is larger than the maximum value of the colour bar, so they are excluded. The white points lie outside the parameter ranges of consideration, and therefore they have not been computed. For instance, we see a white band for small m_Y because their values lie below the lower bound 0.1 TeV. Other important features displayed in all the plots are the solid red and blue lines representing the 1-σ and 2-σ contours. These lines define the boundaries of the regions where $\Delta\chi^2 \leq 2.30$ and $\Delta\chi^2 \leq 5.99$, respectively. In other words, all the points within the red contour are allowed at 68% confidence level (1-σ), while those within the blue contour correspond to the 95% confidence level (2-σ) .

Another thing to bear in mind is that the calculations might not be adequate if the width of the mediator is too large. Dijet and dilepton searches are resonance searches, and they study the invariant

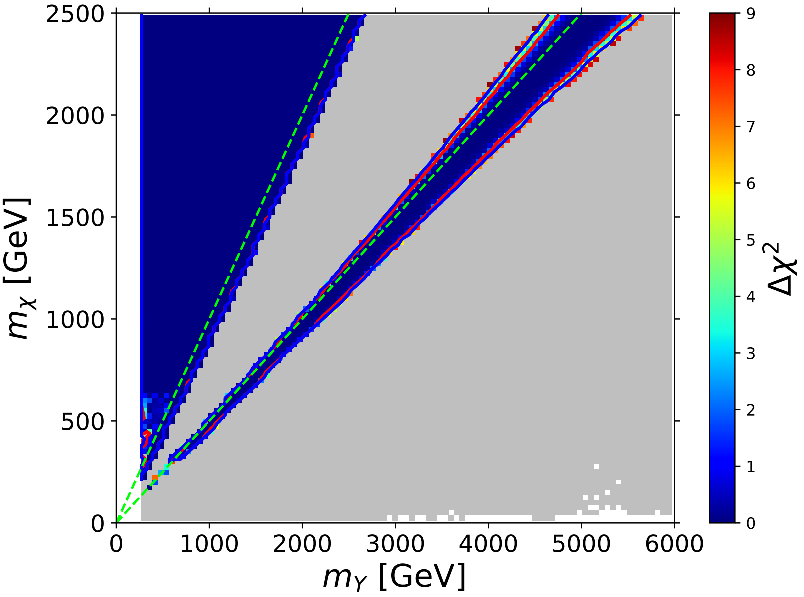

Figure 5.1: Likelihood function in the (m_Y, m_χ) plane with the additional constraints on the total mediator width $\Gamma_Y/m_Y < 0.1$ and on the lepton coupling $g_l < 0.001$. The figure is coloured according to the values of $\Delta\chi^2 = \chi^2 - \chi^2_{\text{min}}$, and the points for which $\Delta\chi^2 > 9$ are displayed in grey. The white band for small values of m_Y shows the points that have not been computed because they lay outside the consideration range for m_Y: (0.1, 6) TeV. The 1-σ and 2-σ regions are delineated by red and blue contours, respectively. The top dashed line corresponds to the points where $m_Y = m_\chi$, and the bottom dashed line shows the condition $m_Y = 2m_\chi$.

mass spectrums of the events[12]. Experimentally, we observe the mediator resonance, but if the width of such resonance were too large, it would be indistinguishable from the background. Consequently, the searches would not be sensitive enough, and we could not use them to impose bounds. We avoid this limitation by enforcing a cut on the ratio Γ_Y/m_Y. For instance, in previous works with `MasterCode`, the cut imposed was $\Gamma_Y/m_Y < 0.3$. However, in this work, we are adding a new decay channel by allowing g_l to be greater than zero, and we have also included the latest dilepton searches as experimental constraints. Hence, as these dilepton results are available from ATLAS only up to a ratio $\Gamma_Y/m_Y = 0.1$, we must use this bound to be consistent with the experimental analyses [34]. Figure 5.2 shows an example to understand how Γ_Y/m_Y is involved in the calculations. It displays the (m_Y, m_χ) plane coloured according to the values of $\Delta\chi^2$ for four different upper limits on Γ_Y/m_Y. In particular, the dark blue points are allowed as they lay inside the contours and satisfy all the model constraints. The top dashed line in the plots corresponds to the condition $m_Y = m_\chi$, and the bottom dashed line shows the condition $m_Y = 2m_\chi$. These lines are not of major importance at the moment, as we will discuss them later, but for now, they are useful to guide us in comparing the plots. We observe that the higher Γ_Y/m_Y is accepted, the more the allowed area is extended downwards. In other words, the points where $m_Y > m_\chi$ tend to have a relatively large Γ_Y/m_Y, as the more we restrict the cut, the more the region is suppressed. Still, the points where $2m_\chi > m_Y$ are always allowed, no matter how low the cutoff value for Γ_Y/m_Y is. Note that in figures 5.2a and 5.2b, we observe some white points mixed with the grey ones. In this case, unlike what was discussed above, they are not outside the ranges of consideration but appear due to low

---

[12] The invariant mass characterises the energy and momentum of a system, and it is the same in every reference frame. The distribution of this quantity for a certain number of events is what we call the invariant mass spectrum of the system.

sampling statistics. We only observe such white regions for the upper bounds $\Gamma_Y/m_Y < 0.01$ and $\Gamma_Y/m_Y < 0.05$, which are very restrictive, thus significantly reducing the number of sampled points. Therefore, when we run the fit on these points, convergence problems arise, and, as a result, they are not computed. As we allow higher values for Γ_Y/m_Y, we observe that the whole region is covered. Running a dedicated sampling for low Γ_Y/m_Y values would be advisable if we wanted to recover all these points. In all the following plots, we use the constraint $\Gamma_Y/m_Y < 0.1$. Hence, whenever the $(m_Y,\, m_\chi)$ plane is displayed, we will observe the same contours as in figure 5.2c.

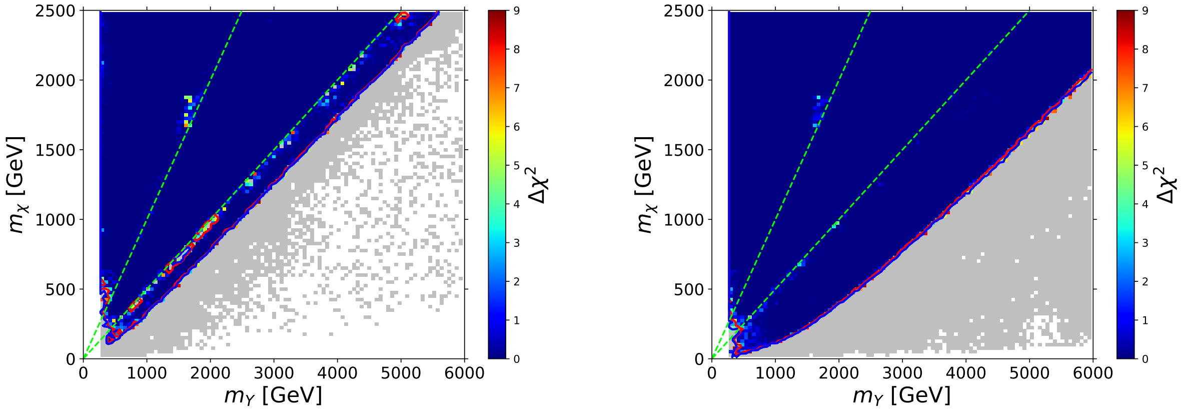

(a) $\Gamma_Y/m_Y < 0.01$

(b) $\Gamma_Y/m_Y < 0.05$

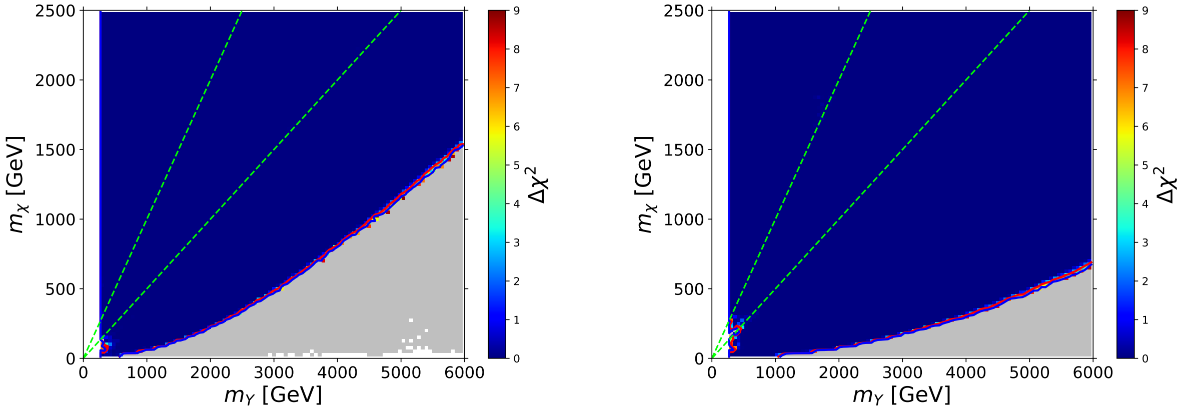

(c) $\Gamma_Y/m_Y < 0.1$

(d) $\Gamma_Y/m_Y < 0.3$

Figure 5.2: Comparison of the likelihood functions in the $(m_Y,\, m_\chi)$ plane for different upper bounds on the total mediator width Γ_Y/m_Y. Top left: $\Gamma_Y/m_Y < 0.01$. Top right: $\Gamma_Y/m_Y < 0.05$. Bottom left: $\Gamma_Y/m_Y < 0.1$. Bottom right: $\Gamma_Y/m_Y < 0.3$. All the figures are coloured according to the values of $\Delta\chi^2 = \chi^2 - \chi^2_{\text{min}}$, and the points for which $\Delta\chi^2 > 9$ are displayed in grey. The white band for small values of m_Y shows the points that have not been computed because they lay outside the consideration range for m_Y: (0.1, 6) TeV. The 1-σ and 2-σ regions are delineated by red and blue contours, respectively. The top dashed line corresponds to the points where $m_Y = m_\chi$, and the bottom dashed line shows the condition $m_Y = 2m_\chi$.

Furthermore, it is interesting to remark how the cut on Γ_Y/m_Y implicitly restricts g_l. In figure 5.3, we represent Γ_Y/m_Y versus g_l to observe how larger values of g_l are excluded as Γ_Y/m_Y decreases.

Mathematically, we see this in equation 2.1:

$$\Gamma_Y^{l\bar{l}} = \frac{g_l^2 m_Y}{12\pi}\left(1 + \frac{2m_l^2}{m_Y^2}\right)\sqrt{1 - \frac{4m_l^2}{m_Y^2}}.$$

The most important conclusion we draw from this figure is the following. Since the cutoff applied throughout this work is $\Gamma_Y/m_Y < 0.1$, we implicitly limit g_l to the range (0, 2.8), as seen from the green dashed line in the plot.

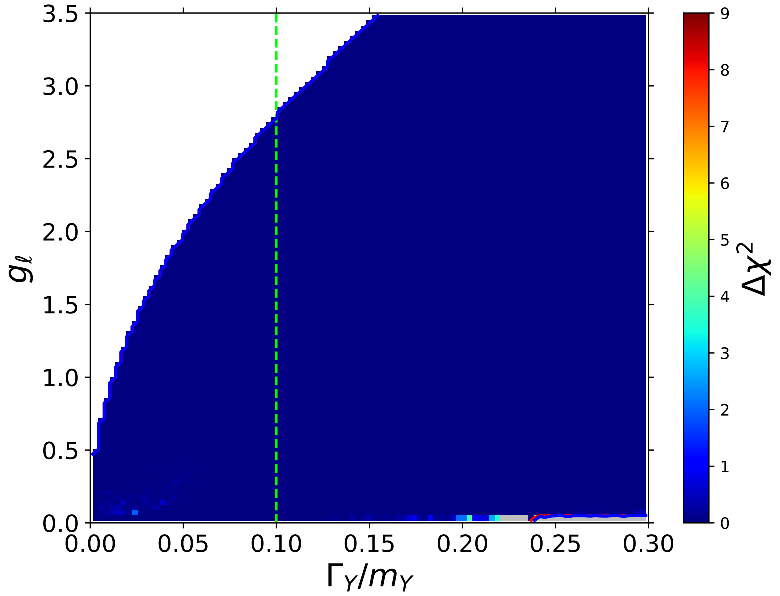

Figure 5.3: Likelihood function in the $(\Gamma_Y/m_Y,\ g_l)$ plane. The figure is coloured according to the values of $\Delta\chi^2 = \chi^2 - \chi^2_{\text{min}}$. The 1-$\sigma$ and 2-σ regions are delineated by red and blue contours, respectively. The dashed vertical line corresponds to the points where $\Gamma_Y/m_Y = 0.1$, which is the cut applied throughout this work.

5.2 Discussion of results

The database generated after the first sampling has $\sim$ 192 million points. From this database, I have run the profilings of the likelihood functions with the ranges shown in table 4.1 and the set of constraints in chapter 3. It is also important to remark that all the results have been computed with `MasterCode` considering the theoretical model with the parameters described above and a spin-1 vector mediator that couples to leptons. After the profiling, the number of points with $\Delta\chi^2 < 9$ is $\sim$ 34 million.

The first consideration arises when observing an unexpected behaviour for low g_l values in some figures. For instance, figure 5.4a shows the results of the global fit coloured according to the values of $\Delta\chi^2$ as a function of g_l (y-axis) and m_χ (x-axis). We have also considered the additional restriction $\Gamma_Y/m_Y < 0.1$. First, note that g_l is displayed on a logarithmic scale because it helps analyse its behaviour at low values. For $g_l < 10^{-2}$, we observe some non-physical vertical structures that seem to be artificially produced due to a lack of statistics of the samples. In particular, we noticed that g_l was sampled linearly, while the scale shown in the plot is logarithmic, so there is a significant lack of points. We addressed this problem in the following way. First, I have checked that the points inside the columns are good points, which means that the fit has converged correctly and they have a low $\Delta\chi^2$. Then, the idea is to explicitly *deform* the points between the vertical regions, which means slightly varying the three free parameters and computing the remaining observables to see what results they yield. In this way, we want to check whether it is possible to get an acceptable $\Delta\chi^2$ between the columns. For this purpose, I used a script inside `MasterCode`, which allows the user to compute all the observables for a fixed point in the parameter space. Indeed, we found that such good points exist between the vertical structures, thus confirming that the issue was just a sampling artefact caused by the lack of statistics rather than a model feature. To fix this, we needed to run a dedicated sampling in the subspace of low g_l to recover the missing points. The ranges for g_l chosen for the new boxes are (10^{-2} - 10^{-6}) on a logarithmic scale and (10^{-6} - 0) on a linear scale. With this new sampling, which has $\sim$ 8 million new points, we expected to compute the empty bins and get a correct fit in all the parameter space. Indeed, in figure 5.4b, we observe that the entire space is covered.

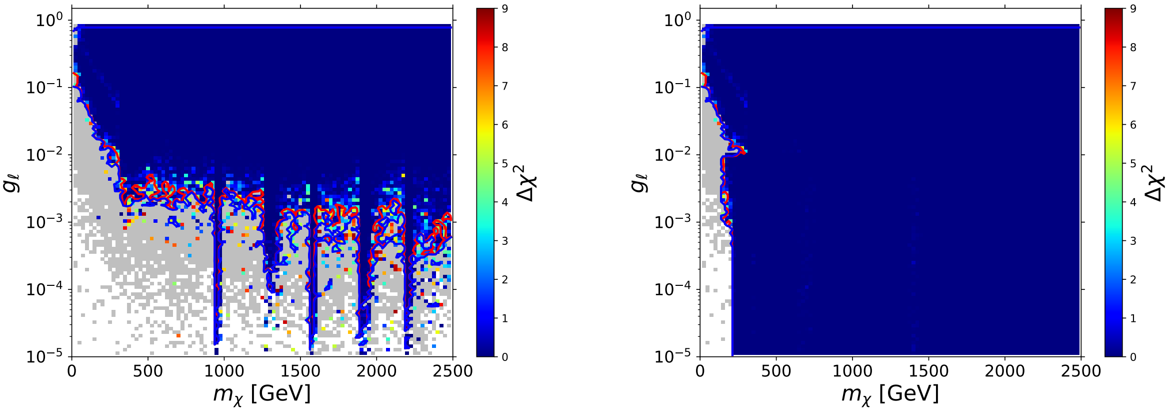

(a)

(b)

Figure 5.4: Comparison of the likelihood function in the (m_χ, g_l) plane with the additional constraint $\Gamma_Y/m_Y < 0.1$. Left: first sampling ($\sim$ 192 million points). Right: first sampling merged with the dedicated one in the subspace of low g_l ($\sim$ 8 million points). Note that the y-axis, g_l, is shown on a logarithmic scale. Both plots are coloured according to the values of $\Delta\chi^2 = \chi^2 - \chi^2_{\rm min}$, and the points for which $\Delta\chi^2 > 9$ are displayed in grey. The 1-σ and 2-σ regions are delineated by red and blue contours, respectively.

5.2.1 (m_Y, m_χ)

First, we want to verify if the results obtained are consistent with the published ones in [21]. The difference between the two studies lies in allowing the mediator coupling to leptons or not. Hence, our first approach is to perform a new profiling with the condition $g_l < 0.001$ and compare it with the published results, for which g_l is zero. Figure 5.5 shows the (m_Y, m_χ) plane for the leptophobic scenario (left) and the leptophilic scenario with the upper bound $g_l < 0.001$ (right). The white band for small values of m_Y shows the points that have not been computed because they lay outside the consideration range for m_Y: (0.1,6) TeV. The remaining white regions are excluded because their χ^2 is too large. In fact, they correspond to the grey points in 5.2c. The top dashed line in the right figure corresponds to the points where $m_Y = m_\chi$, and the bottom dashed line shows the condition $m_Y = 2m_\chi$. Both figures are coloured according to the dominant DM annihilation mechanism that minimizes χ^2: t-channel annihilation in green and s-channel annihilation in yellow. At the moment, we only look at the regions that are allowed, regardless of the colour, as we will give more information on the mechanisms below. Comparing both plots, we conclude that we reproduce the published results for this plane when imposing the upper bound $g_l < 0.001$.

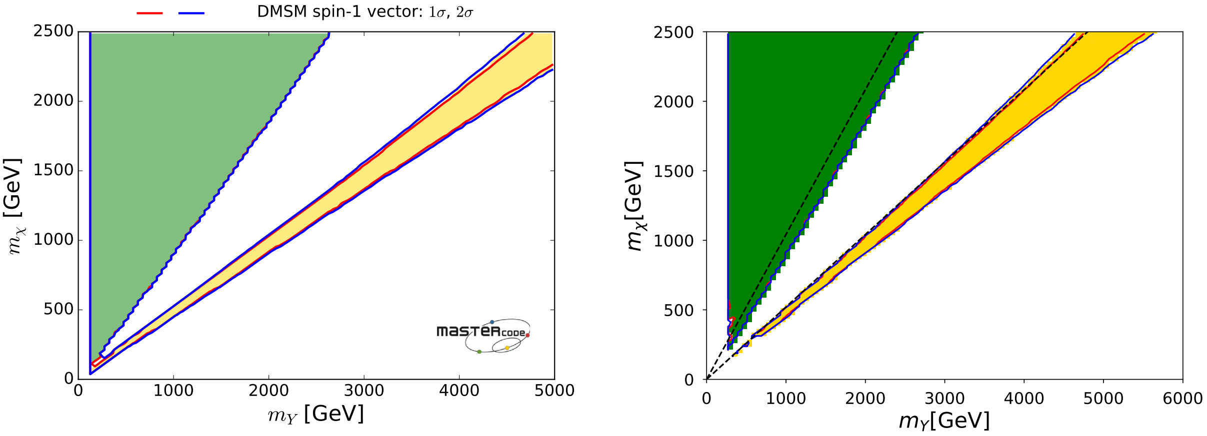

(a) $g_l = 0$

(b) $g_l < 0.001$

Figure 5.5: Comparison of the likelihood functions in the (m_Y, m_χ) plane. Left: leptophobic scenario ($g_l = 0$) from [21]. Right: leptophilic scenario with $g_l < 0.001$. Both figures are coloured according to the dominant mechanism for the DM annihilation at each allowed region: t-channel annihilation in green and s-channel annihilation in yellow. The white band for small values of m_Y shows the points that have not been computed because they lay outside the consideration range for m_Y: (0.1, 6) TeV. The remaining white regions are excluded regions because their χ^2 is too large. In fact, they correspond to the grey points in 5.2c. The 1-σ and 2-σ regions are delineated by red and blue contours, respectively. The top dashed line corresponds to the boundary of the t-channel region, $m_Y = m_\chi$, and the bottom dashed line shows the condition $m_Y = 2m_\chi$.

In figure 5.6, we analyse how the parameter space varies as g_l is increasingly allowed. For this purpose, we display the results for two profilings with fixed upper bounds $g_l < 0.01$ and $g_l < 0.1$, and a third profiling with no cut on g_l. It is important to remark that the cut $\Gamma_Y/m_Y < 0.1$ is imposed in the three plots, which means that, as we saw in figure 5.3, g_l is implicitly restricted to $g_l \lesssim 2.8$. The figures are coloured according to the mechanism that dominates in each region of the space: yellow for the s-channel and green for the t-channel. In figures 5.6b and 5.6c, the 1-σ and 2-σ contours are mostly overlapped, meaning there is no significant region with points lying outside the 68% region and inside the 95%. Comparing the three plots, the most remarkable feature we observe is that the allowed region is extended as we allow larger values for g_l. On the one hand, the white triangle between the two regions in figure 5.5a, $m_\chi < m_Y < 2m_\chi$ (i.e. the region between the two dashed lines) is allowed in figures 5.6b and 5.6c. On the other hand, we appreciate that the contours move progressively downwards as we allow larger values of g_l. In particular, in figure 5.6c, the whole range of m_Y is allowed for $m_\chi > 1500$ GeV. However, the larger m_Y, the more m_χ is constrained to higher values. For instance, when $m_Y \sim 1000$ GeV, the minimum value that is allowed for m_χ is ~ 50 GeV and when $m_Y \sim 5000$ GeV, we need to go up to $m_\chi > 1200$ GeV to be inside the contours.

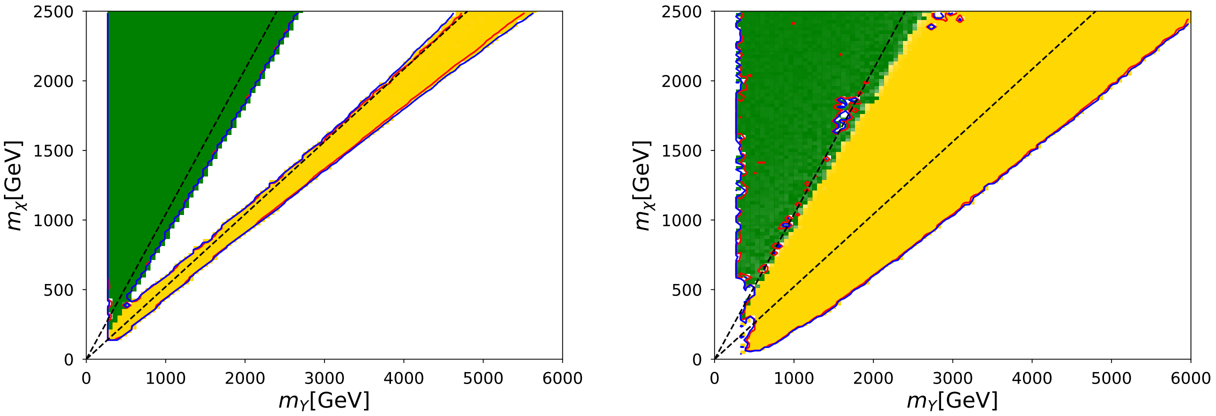

(a) $g_l < 0.01$ (b) $g_l < 0.1$

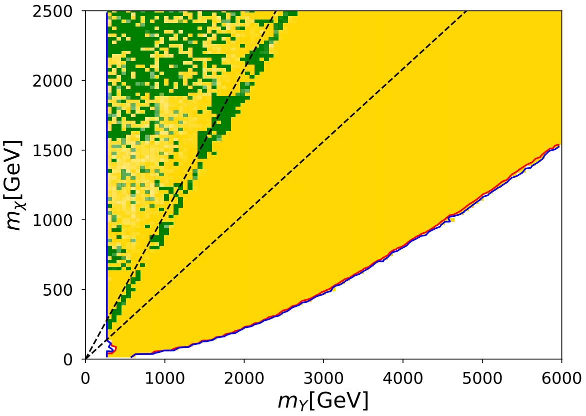

(c) $\Gamma_Y/m_Y < 0.1$

Figure 5.6: Comparison of the likelihood functions in the (m_Y, m_χ) plane for different upper bounds on the lepton coupling g_l and the additional constraint $\Gamma_Y/m_Y < 0.1$. Top left: $g_l < 0.01$. Top right: $g_l < 0.1$. Bottom: $\Gamma_Y/m_Y < 0.1$. All the figures are coloured according to the dominant mechanism for the DM annihilation at each allowed region: t-channel annihilation in green and s-channel annihilation in yellow. The intensity of the colour depends on how dominant the mechanism is. The white band for small values of m_Y shows the points that have not been computed because they lay outside the consideration range for m_Y: (0.1, 6) TeV. The remaining white regions are excluded regions because their χ^2 is too large. The 1-σ and 2-σ regions are delineated by red and blue contours, respectively. The top dashed line corresponds to the boundary of the t-channel region, $m_Y = m_\chi$, and the bottom dashed line shows the condition $m_Y = 2m_\chi$.

At this point, we are interested in understanding why as g_l increases, we obtain new allowed areas. For this purpose, the previous figures are coloured according to the mechanism that dominates at each region of the space. The four possible DM annihilation mechanisms are shown below in figure 5.7. Note that since our study is flavour-independent, we write l^-, l^+ for general leptons and their antiparticles, and q, $\bar{q}$ for general quarks and antiquarks. However, we only distinguish whether the decay is through the t-channel (right) or s-channel (left), regardless of whether it decays to quarks or leptons. The process to determine such dominant mechanisms is the following. `micrOMEGAs` stores the percentages of how much each channel contributes to the total DM annihilation at each point in the plane. Hence, from this information, the points where the s-channel is the dominant mechanism are shown in yellow, and those where the dominant mechanism is the t-channel are coloured in green.

Moreover, the intensity of the colour depends on how dominant the mechanism is, as we can observe in figure 5.6c. It is also important to clarify that the fact that one region is coloured in green does not mean that the t-channel is the only possible mechanism, but that, for the points that minimise χ^2, it dominates over the s-channel. The same is true for the yellow region.

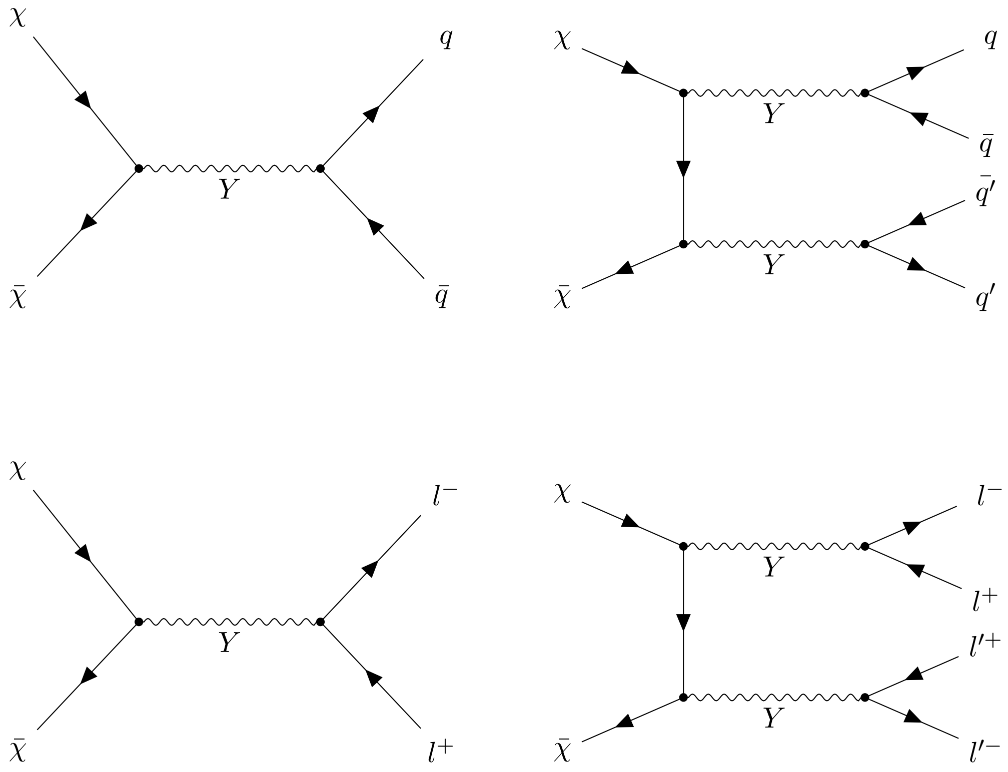

Figure 5.7: Feynman diagrams for the two processes contributing to DM annihilation: the annihilation through a single mediator in the s-channel (left) and the t-channel annihilation to a pair of mediators that subsequently decay to quarks (right). Y denotes a general mediator particle and χ ($\bar{\chi}$) the DM particles (antiparticles), while q and q' (l^- and l'^-) represent two general quarks (leptons), with $\bar{q}$ and $\bar{q}'$ (l^+ and l'^+) denoting their respective antiparticles.

Consider again figures 5.5 and 5.6. As mentioned before, the allowed regions in these plots are coloured according to the dominant mechanism for the DM decay that gives the smallest χ^2: s-channel in yellow and t-channel in green. In figures 5.5b and 5.6a, we observe that above the condition $m_\chi > m_Y$, the region is green, while the other allowed region is coloured in yellow. There are no significant differences between these two figures, except that in the second one, there are more allowed points at low values for the masses. When we restrict our parameter space too much, as in 5.5b, we cannot find allowed points in such region. However, for $g_l < 0.01$, the `MultiNest` algorithm finds more points, and it is covered. Concerning the green region, it remains unchanged in 5.6b, but it slightly disappears in 5.6c as g_l is increasingly allowed, and we observe a mix of the two mechanisms being dominant. The reason is that, as we mentioned earlier, we take for each bin a single point that corresponds to the lowest χ^2. Hence, in this region, we have a slightly lower χ^2 with one mechanism than the other, but it is simply numeric. The result is an overlap of the mechanisms as both are equally probable. Regarding the new allowed region in figures 5.6b and 5.6c, where $m_\chi < m_Y < 2m_\chi$ (i.e. the region between the two dashed lines), the mechanism that dominates is the s-channel. The same is true for the extended area below the bottom dashed line.

For more information on the mechanisms that dominate in each region of the (m_Y, m_χ) plane, figure 5.8 represents the values of the couplings on colour scale: g_χ (top left), g_q (top right) and g_l (bottom). Observe that the colour bar has a different range for each coupling. In particular, note that the g_l colour bar has its maximum value at 0.5. It is shown this way in order to better visualise how g_l changes in the different regions of the plane, but we should keep in mind that g_l is allowed up to ~ 2.8, as we saw in figure 5.3. Starting with the region $m_\chi > m_Y$, we observe that we have extremely small values of g_q ($< 10^{-5}$), while g_l is allowed in the range (0 - 0.7) and g_χ in (0.3 - 1.1). Recall that in this model we are using dijet and dilepton constraints from the LHC. The results from dijet searches are translated into upper bounds on g_q and on the production cross-section. Indeed, such constraints are very effective in suppressing g_q, in particular for low values of m_Y [21]. Therefore, it seems that in order to have a relevant annihilation cross-section for the decay to leptons, we must reduce the annihilation cross-section for the decay to quarks, which means suppressing g_q. Concerning the adjacent region, $m_\chi < m_Y < 2m_\chi$ (forbidden in the leptophobic scenario), we observe that g_q is still very small and g_l has decreased (<0.15), while g_χ, on the contrary, has increased (>1.8). Checking the stored values in the database, we see that we need $g_l > 0.05$ for this region to be allowed, but the values that give the lowest χ^2 are not particularly large: $g_l \in (0.05,\ 0.15)$. Therefore, we can conclude that allowing g_l to be non-zero makes this region accessible, even if g_l is not too high, as seen in figure 5.6b. As a consequence, g_q and g_χ are modified, reducing the decay to quarks and enlarging the coupling to DM. Such low values of g_q and g_l restrict the corresponding annihilation cross section to very small values. In equation 1.2 we observed that the annihilation cross-section σ_{ann} is inversely proportional to $\Omega_\chi h^2$:

$$\Omega_\chi h^2 = \frac{m_\chi}{\rho_c} \frac{H_0}{\langle \sigma_{\text{ann}} v \rangle} h^2$$

hence the suppression of such cross-sections results in an enhancement of the relic density. To compensate for this, it seems that g_χ must be increased so that the annihilation cross section is high enough to lower the computed value for the relic density and effectively reproduce the observed one. Finally, at $m_Y > 2m_\chi$, the values for the couplings remain approximately the same as in the previous region and, as they approach the contour lines, both g_l and g_q increase. As a result, following the same reasoning as before, g_χ decreases to give the correct value for the relic density.

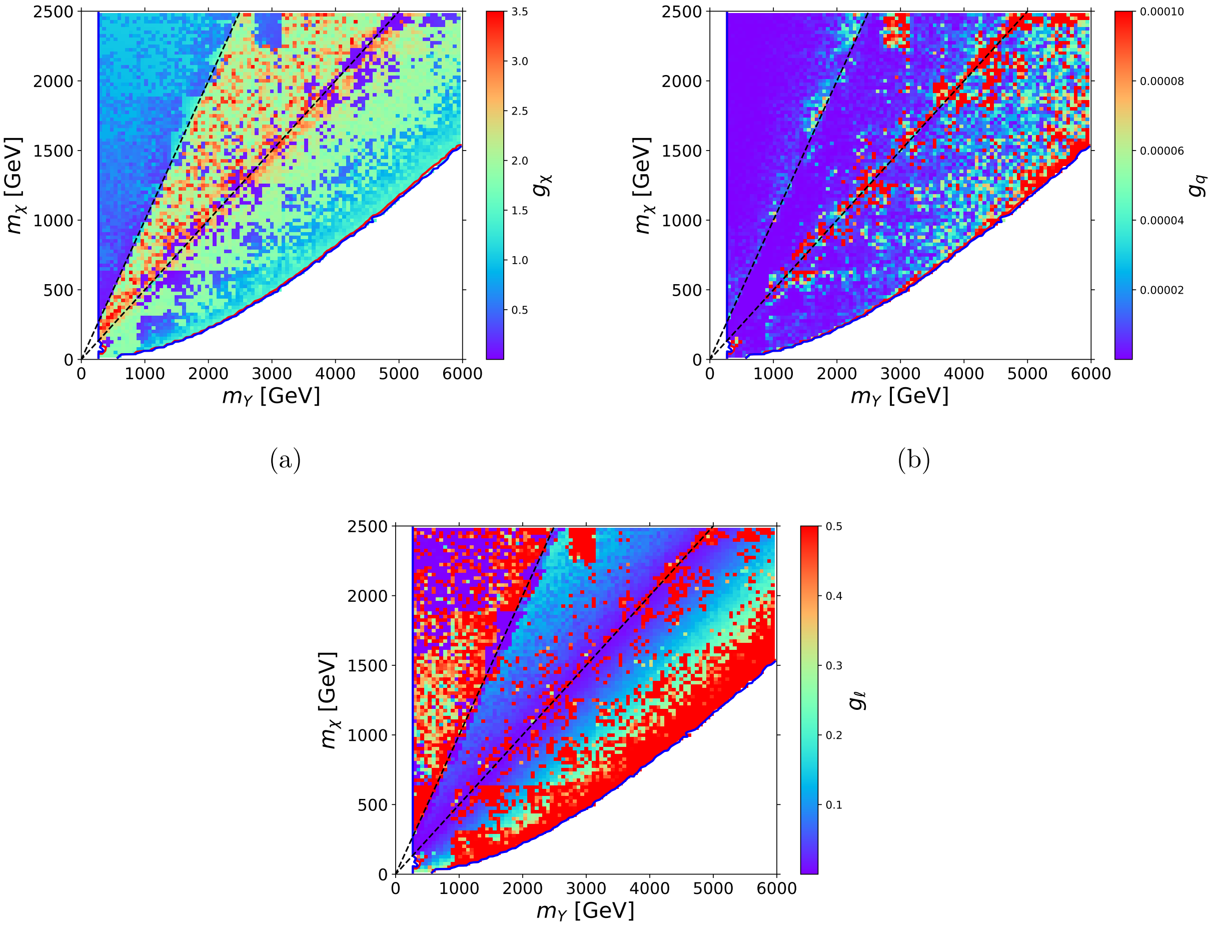

(a) (b)

(c)

Figure 5.8: Comparison of the likelihood functions in the $(m_Y,\ m_\chi)$ plane with the additional constraint $\Gamma_Y/m_Y < 0.1$. Top left: coloured according to the values of g_χ. Top right: coloured according to the values of g_q. Bottom: coloured according to the values of g_l. Note that the colour scale has a different range for each coupling. The white bands for small values of m_Y show the points that have not been computed because they lay outside the consideration range for m_Y: (0.1, 6) TeV. The white regions below the contours correspond to the grey region in figure 5.2c, where the χ^2 is too large, so it is excluded. The 1-σ and 2-σ regions are delineated by red and blue contours, respectively. The top dashed line corresponds to the boundary of the t-channel region, $m_Y = m_\chi$, and the bottom dashed line shows the condition $m_Y = 2m_\chi$.

In figure 5.9, we continue the analysis of the same plane in terms of the total and partial decay widths. The figures are coloured according to the values of the total width, Γ_Y/m_Y (bottom), the partial width to SM particles $\Gamma_Y^{\mathrm{SM}}/m_Y = (\sum_q \Gamma_Y^{q\bar{q}} + \sum_l \Gamma_Y^{ll})/m_Y$ (top right) and the partial width to DM particles $\Gamma_Y^{\mathrm{DM}}/m_Y$ (top left), with the additional restriction $\Gamma_Y/m_Y < 0.1$. Consider the equation 2.1 shown in chapter 2 for the mediator decay width:

$$\Gamma_Y = \Gamma_Y^{\mathrm{DM}} + \Gamma_Y^{\mathrm{SM}} = \Gamma_Y^{\chi\bar{\chi}} + \sum_q \Gamma_Y^{q\bar{q}} + \sum_l \Gamma_Y^{ll}$$

and recall that it depends on all the parameters of our model. Therefore, allowing $g_l > 0$ means that the total width for the leptophilic scenario is larger than for the leptophobic one, as Γ_Y^{ll}=0 when g_l=0. Now, if we impose a cutoff on Γ_Y/m_Y, the three decay modes are constrained to satisfy the condition. Let us start with figure 5.9a and the region $2m_\chi > m_Y$. Checking explicitly such values in the database, it turns out that the values for $\Gamma_Y^{\mathrm{DM}}/m_Y$ are of the order of 10^{-11}, which means that the mediator decay to DM is mostly suppressed in this region. This is what we would expect if we take into account that in this region the decay of the mediator to a pair of DM particles is forbidden by the kinematic constraint $m_Y < 2m_\chi$. For this reason, the contribution to the total width in this area comes exclusively from the decay to SM particles: $\Gamma_Y^{\mathrm{SM}}/m_Y \in (10^{-15}, 0.1)$. Below the bottom dashed line, the decay to DM particles predominates over the decay to SM.

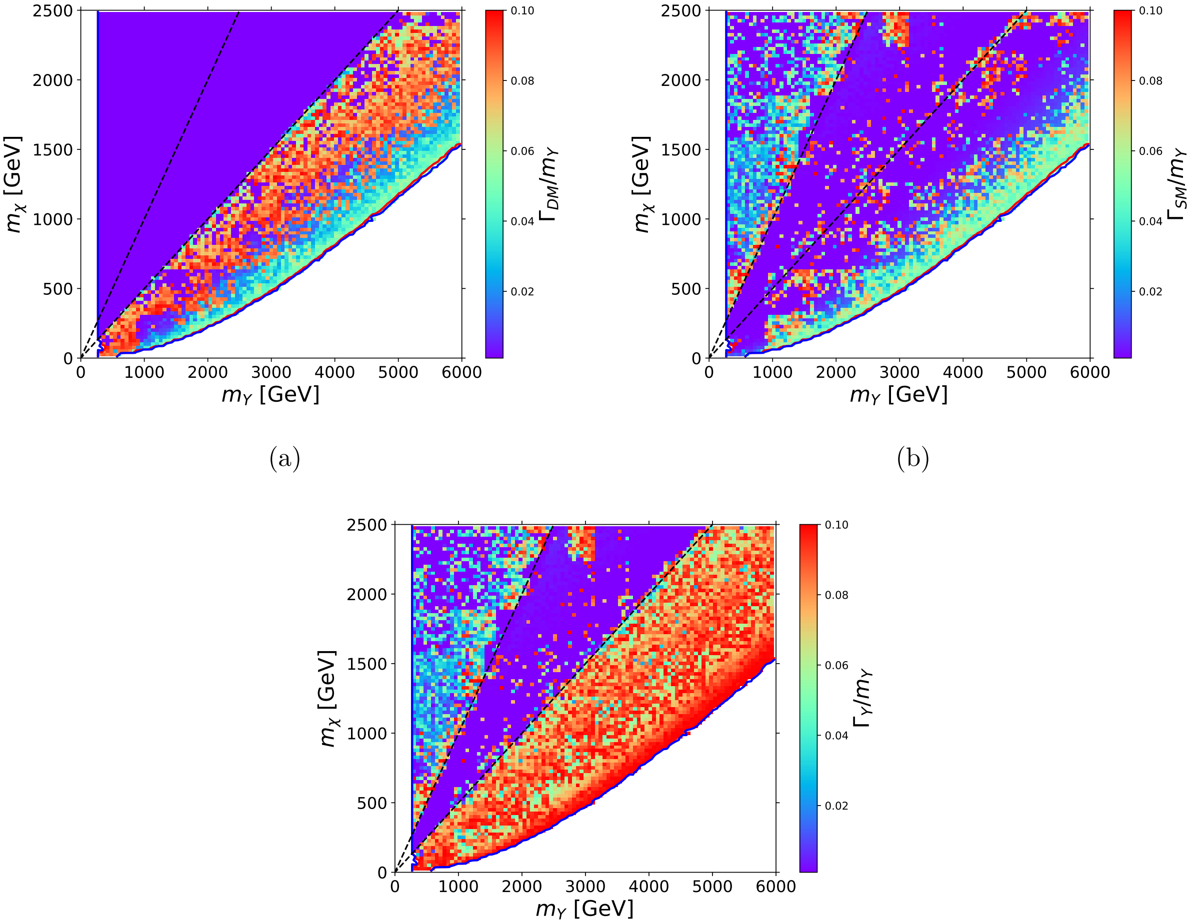

(a)

(b)

(c)

Figure 5.9: Comparison of the likelihood functions in the (m_Y, m_χ) plane with the additional constraint $\Gamma_Y/m_Y < 0.1$. Top left: coloured according to the values of the partial width $\Gamma_Y^{\mathrm{DM}}/m_Y$. Top right: coloured according to the values of the partial width $\Gamma_Y^{\mathrm{SM}}/m_Y = (\sum_q \Gamma_Y^{q\bar{q}} + \sum_l \Gamma_Y^{ll})/m_Y$. Bottom: coloured according to the values of the total width Γ_Y/m_Y. The white bands for small values of m_Y show the points that have not been computed because they lay outside the consideration range for m_Y: (0.1, 6) TeV. The white regions below the contours correspond to the grey region in figure 5.2c, where the χ^2 is too large, so it is excluded. The 1-σ and 2-σ regions are delineated by red and blue contours, respectively. The top dashed line corresponds to the boundary of the t-channel region, $m_Y = m_\chi$, and the bottom dashed line shows the condition $m_Y = 2m_\chi$.

To understand how the relic density constraint affects the parameter space, we are interested in reproducing the previous plots in terms of $\Omega_\chi h^2$. Recall the correct value for the relic density given in equation 1.1: $\Omega_\chi h^2 = 0.118 \pm 0.001$. Figure 5.10 displays the (m_Y, m_χ) plane coloured as a function of the values of $\Omega_\chi h^2$. As mentioned before, each point in the plane has fixed values for m_Y and m_χ, whereas the three mediator couplings are the free parameters. Hence, the various combinations of the couplings give different values of χ^2 and $\Omega_\chi h^2$. The colour coding shows the relic density values for the points that yield the smallest χ^2 at each pair (m_Y, m_χ). It is important to remark that χ^2 and $\Omega_\chi h^2$ are not independent. Since the relic density is one of the constraints of our model, every point that is allowed (i.e. gives a low χ^2) must have a value of $\Omega_\chi h^2$ close to the measured one. Otherwise, χ^2 would be large, and it would be excluded. However, we could have points that predict the correct value yet are excluded by other constraints. Therefore, for all the green points in the allowed region of the plane, there is at least one combination of g_q, g_l and g_χ that gives a low χ^2 and, in particular, predicts the correct value of $\Omega_\chi h^2$. Indeed, we remark that for all the points inside the contours in figure 5.10, including the new allowed areas, we perfectly reproduce the observed value within the margin of error. Outside these contours, the regions are not allowed anymore. Some excluded points are displayed in dark red to observe that as soon as $\Omega_\chi h^2$ is larger than the measured value, the points give a large $\Delta\chi^2$ and the region falls below the contours. This leads us to conclude that what drives the exclusion in this region is not the collider constraints but the relic density. In fact, below the bottom dashed line, we enter the region where $m_Y > 2m_\chi$ and the DM annihilation via the mediator is increasingly suppressed as we move far from the dashed line. Hence the suppression of such cross-section results in an enhancement of the relic density, and the region becomes excluded.

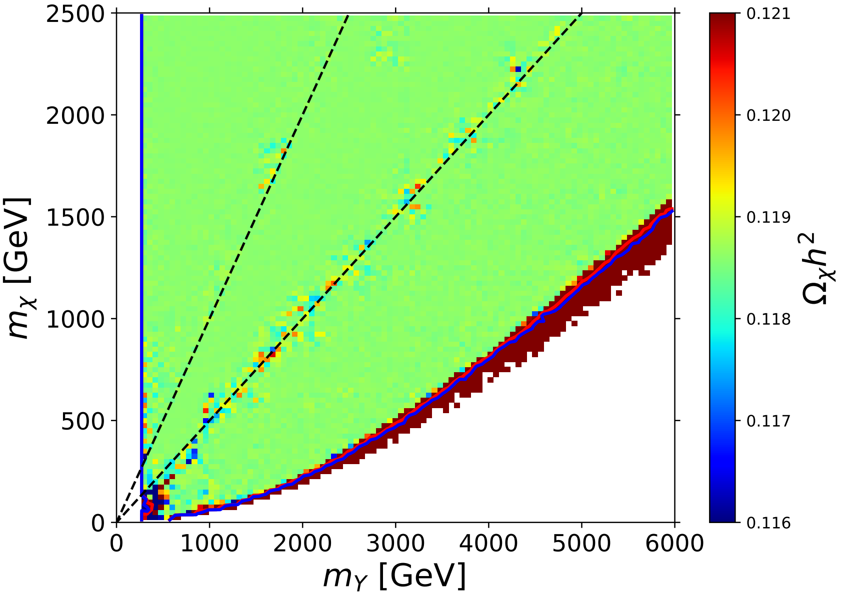

Figure 5.10: Likelihood function in the (m_Y, m_χ) plane coloured according to the values of the relic density $\Omega_\chi h^2$, with the additional constraint $\Gamma_Y/m_Y < 0.1$. The white band for small values of m_Y shows the points that have not been computed because they lay outside the consideration range for m_Y: (0.1, 6) TeV. The white regions below the contours correspond to the grey region in figure 5.2c, where the χ^2 is too large, so it is excluded. The 1-σ and 2-σ regions, are delineated by red and blue contours, respectively. The top dashed line in the plot corresponds to the boundary of the t-channel region, $m_Y = m_\chi$, and the bottom dashed line shows the condition $m_Y = 2m_\chi$.

With the analysis in this plane, we reach to some conclusions. First, that we effectively reproduce the published results in [21] when we impose $g_l < 0.001$. Second, that increasing g_l to be non-zero results in an enlargement of the allowed region that predicts the correct value for the relic density and is dominated by the s-channel mechanism. Moreover, in the region $m_\chi > m_Y$, where the t-channel dominated for $g_l = 0$, the s-channel becomes equally probable for $g_l > 0.1$, and we see a mix of the two mechanisms being dominant. Regarding the couplings, the fact that g_l is non-zero causes g_q to be suppressed in the whole plane, which means that the decay to quarks is reduced as the decay to leptons is increasingly enhanced. Another feature of interest in this plane is that the the contours are very close to each other. This means that there is a large allowed region with $\Delta\chi^2 \ll 1$ (in dark blue) and a very steep rise of $\Delta\chi^2$ where the points are not allowed anymore as they become rapidly excluded by any of the constraints. Finally, we have observed that the DM relic density is a strongly constraining observable since we find overabundance as soon as we move outside the observed value and the χ^2 becomes very large. The next step is to analyse other regions of the parameter space.

5.2.2 (g_q, g_χ), (m_χ, g_q), (m_Y, g_q), (m_χ, g_χ) and (m_Y, g_χ)

Figure 5.11 displays the $(g_q,\, g_\chi)$ plane coloured according to $\Delta\chi^2$ for different upper bound values on g_l. The axes are shown on a logarithmic scale. For the limits $g_l < 0.01$ and $g_l < 0.1$, the plots are mainly the same. However, comparing figures 5.11c and 5.11d, it should be noted the allowed region is significantly extended to lower values of g_χ $(0.05 < g_\chi < 0.5)$ as g_l increases, mainly for low values of g_q $(g_q < 10^{-3})$. This leads us to think that such area is only allowed when g_l is sufficiently large. Regarding the subspace where g_χ is large, it is allowed regardless of g_l, and the same applies in the subspace of $g_q > 0.1$. Concerning the four figures, there are some missing points in the region where $g_\chi < 0.5$ and $g_q < 10^{-3}$. A priori, this area falls within the consideration ranges of g_q and g_χ, so it should be covered. The number of sampled points is insufficient to draw conclusions in this parameter region, so we need a dedicated one focusing on such subspace. Nevertheless, the area of most interest in these plots lies between the diagonal lines, which is acceptably covered. The central dotted one shows the region where $g_\chi = g_q$, and the dashed lines at both sides frame the region where $1/3 < g_q/g_\chi < 3$. This choice is because we expect gauge bosons to have similar couplings to the various types of particles based on universality assumptions. This means that we could expect the couplings in our model to be rough of the same order. Taking a look at the central dashed line, such interval is $g_q,\, g_\chi \in (9\cdot 10^{-3}, 0.9)$. The conclusion here is that in order to satisfy the relic density constraint, the couplings cannot be arbitrarily small.

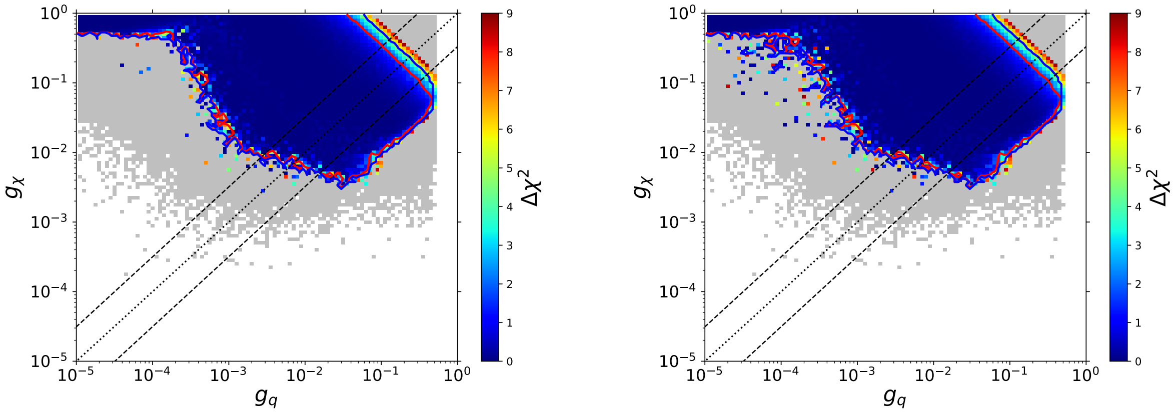

(a) $g_l < 0.001$

(b) $g_l < 0.01$

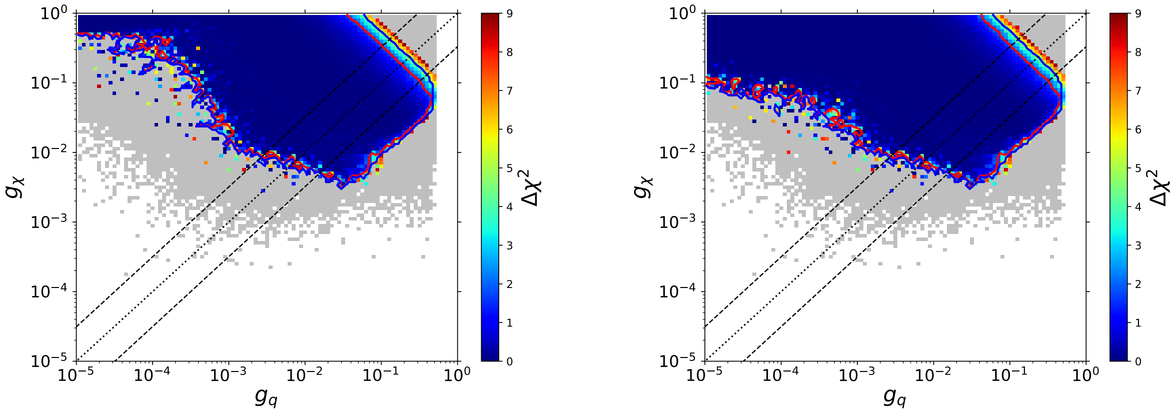

(c) $g_l < 0.1$

(d) $\Gamma_Y/m_Y < 0.1$

Figure 5.11: Comparison of the likelihood functions in the (g_q, g_χ) plane for different upper bounds on the lepton coupling g_l and the additional constraint $\Gamma_Y/m_Y < 0.1$. Top left: $g_l < 0.0001$. Top right: $g_l < 0.01$. Bottom left: $g_l < 0.1$. Bottom right: $\Gamma_Y/m_Y < 0.1$. Note that the axes are shown on a logarithmic scale. All the plots are coloured according to the values of $\Delta\chi^2 = \chi^2 - \chi^2_{\text{min}}$, and the points for which $\Delta\chi^2 > 9$ are displayed in grey. The 1-σ and 2-σ regions are delineated by red and blue contours, respectively. The central dotted line shows the region where $g_\chi = g_q$ and the dashed lines at both sides frame the region where $1/3 < g_q/g_\chi < 3$.

Figure 5.12 displays the (m_χ, g_q) plane, coloured according to $\Delta\chi^2$ for different upper bound values on g_l. The y-axis, g_q, is shown on a logarithmic scale. When we compare the plots, the main feature we observe is that as g_l is enlarged, the region of very low g_q and m_χ is increasingly allowed. In particular, in figure 5.11d, we reach very low values of m_χ, which means that they are only allowed for relatively large values of g_l. Moreover, we appreciate that such low values of m_χ are only allowed when g_q is very small. The reason for this has already been observed before: large values of g_l are allowed when g_q is suppressed. In particular, when $m_\chi < 500$ GeV, there is a steep drop towards very low values of g_q. In the previous figure, we mentioned a problem in the sampling for low values of g_q that showed up as white points in an area that should have been covered. Even if the whole plane is covered in figure 5.12d, it is possible that the number of sampled points is too small, and the program does not converge. Hence, we are missing some points in the region of low values of m_χ and $g_q < 10^{-2}$, which might give a sufficiently low χ^2 that the region is allowed. For this reason, we cannot be sure that the grey area is completely excluded, so a more refined analysis will be needed to conclude this issue. Finally, we observe that for $m_\chi > 800$ GeV, the contours of the allowed region barely change. This means that such an area is allowed as soon as g_l is non-zero, and it remains allowed even if g_l goes up.

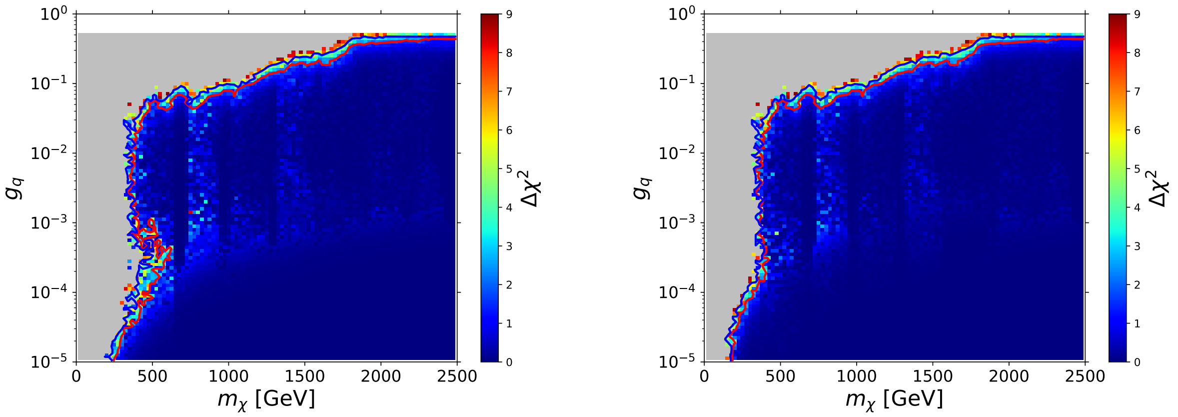

(a) $g_l < 0.001$

(b) $g_l < 0.01$

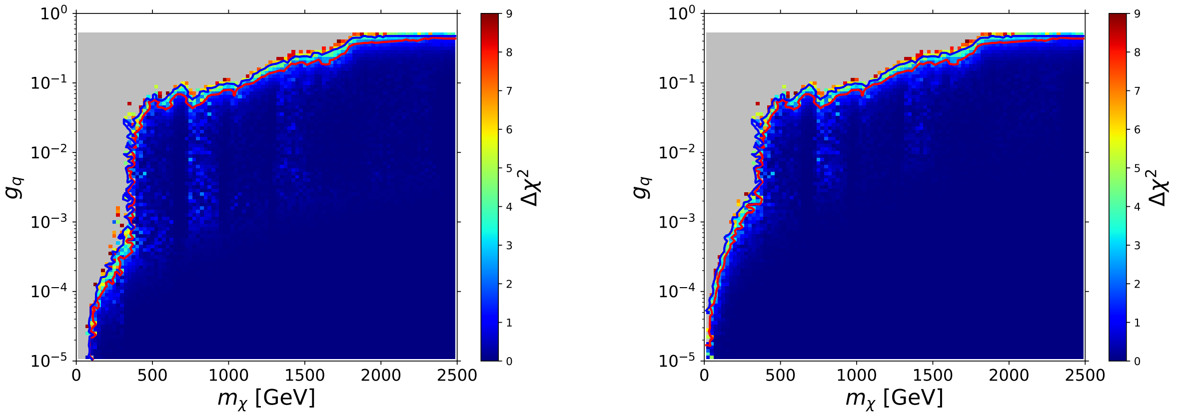

(c) $g_l < 0.1$

(d) $\Gamma_Y/m_Y < 0.1$

Figure 5.12: Comparison of the likelihood functions in the (m_χ, g_q) plane for different upper bounds on the lepton coupling g_l and the additional constraint $\Gamma_Y/m_Y < 0.1$. Top left: $g_l < 0.001$. Top right: $g_l < 0.01$. Bottom left: $g_l < 0.1$. Bottom right: $\Gamma_Y/m_Y < 0.1$. Note that the y-axis is shown on a logarithmic scale. All the plots are coloured according to the values of $\Delta\chi^2 = \chi^2 - \chi^2_{\text{min}}$, and the points for which $\Delta\chi^2 > 9$ are displayed in grey. The 1-σ and 2-σ regions are delineated by red and blue contours, respectively.

Figure 5.13 displays the (m_Y, g_q) plane, coloured according to $\Delta\chi^2$ for different upper bound values on g_l. The y-axis, g_q, is shown on a logarithmic scale. The main feature that stands out is the large excluded region at low values of g_q and $m_Y > 2800$ GeV in figure 5.13a. Indeed, such region is covered as g_l goes up, so we could say that it is accessible when g_l is at least larger than 0.01. Again, from the lack of statistics observed before, we cannot say that the region is completely excluded, as there might be missing allowed points. Hence, it could be possible that it is allowed for very low values of g_l and that we need a dedicated sampling in the lower range of g_q and g_l to observe it. On the contrary, we see that for $g_q > 10^{-3}$, the contours of the allowed region barely change. This means that this region is allowed as soon as g_l is non-zero and it remains allowed even if g_l increases. This figure shows the action of dijet constraints: as m_Y decreases, we need to lower g_q to be allowed. In particular, when g_l is non-zero and $m_Y < 1000$ GeV, there is a steep drop towards very low values of g_q.

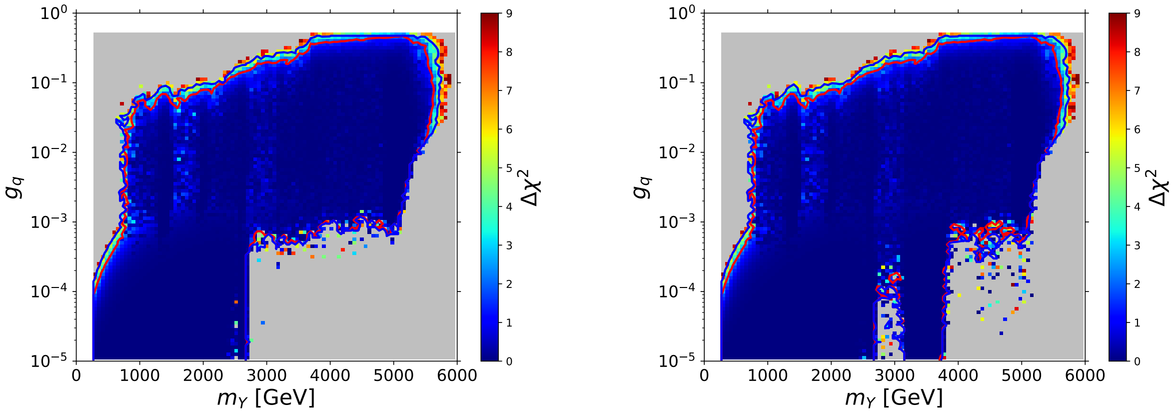

(a) $g_l < 0.001$

(b) $g_l < 0.01$

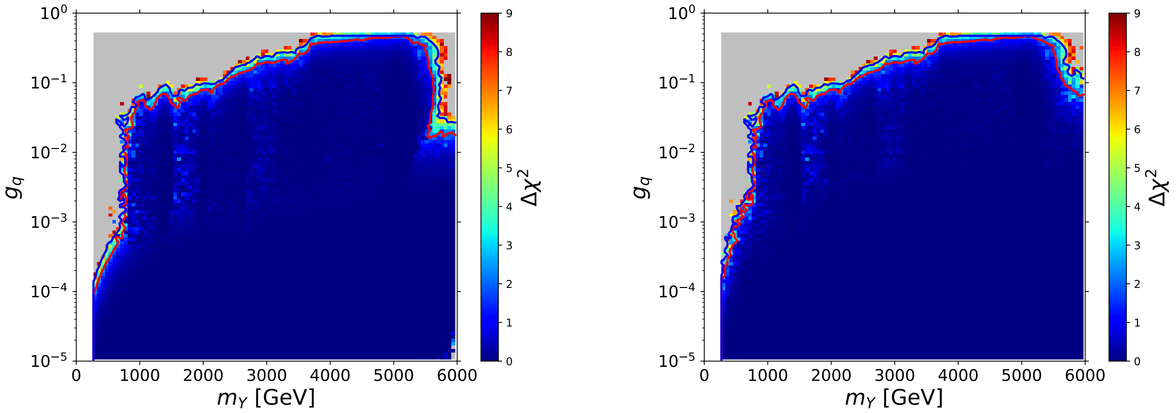

(c) $g_l < 0.1$

(d) $\Gamma_Y/m_Y < 0.1$

Figure 5.13: Comparison of the likelihood functions in the (m_Y, g_q) plane for different upper bounds on the lepton coupling g_l and the additional constraint $\Gamma_Y/m_Y < 0.1$. Top left: $g_l < 0.001$. Top right: $g_l < 0.01$. Bottom left: $g_l < 0.1$. Bottom right: $\Gamma_Y/m_Y < 0.1$. Note that the y-axis is shown on a logarithmic scale. All the plots are coloured according to the values of $\Delta\chi^2 = \chi^2 - \chi^2_{\text{min}}$, and the points for which $\Delta\chi^2 > 9$ are displayed in grey. The 1-σ and 2-σ regions are delineated by red and blue contours, respectively.

Figure 5.14 and 5.15 displays the (m_χ, g_χ) and (m_Y, g_χ) planes, respectively, coloured according to $\Delta\chi^2$ for different upper bound values on g_l. The y-axis, g_χ is shown on a logarithmic scale. The same lack of statistics shown in previous figures is noted here for low values of g_l and especially when $m_\chi < 500$ GeV and $m_Y < 1000$ GeV, respectively. In both figures, we have recovered many points for larger values of g_l (figures 5.14d and 5.15d), but the region of very low g_χ is still missing. Again, the conclusion here is that for low values of m_Y and m_χ, the area is allowed when g_l is at least higher than 0.1. Nevertheless, it is still possible that the upper bounds on g_l restrict the set of sample points too much, so the region is not excluded, but we have not found any allowed points. We would need a dedicated sampling to draw conclusions on this issue. Conversely, the regions where $m_\chi > 500$ GeV, $1000 < m_Y < 5000$ GeV and $g_\chi > 10^{-3}$ are always allowed, regardless of g_l. They are allowed for large values of g_χ because, when g_χ decreases, the χ^2 becomes too large, as a consequence of the annihilation cross-section suppression which results in a relic density overabundance.

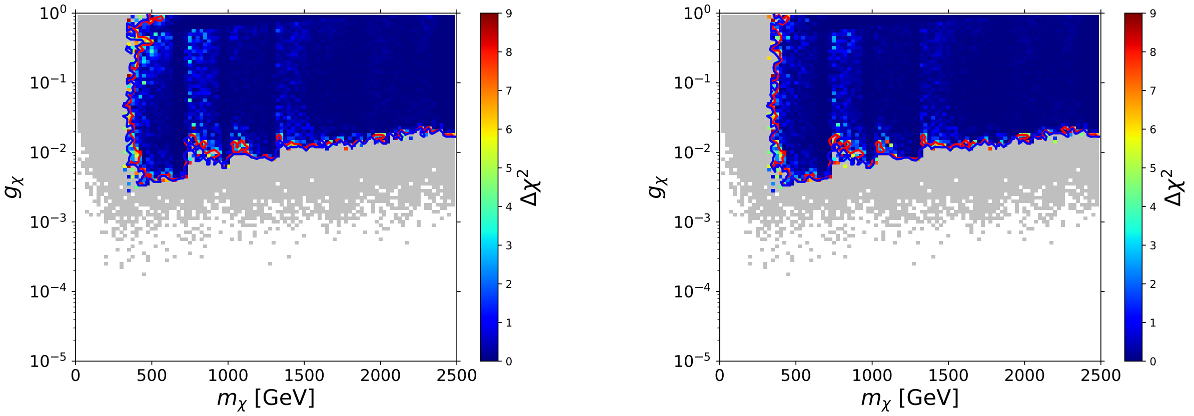

(a) $g_l < 0.001$

(b) $g_l < 0.01$

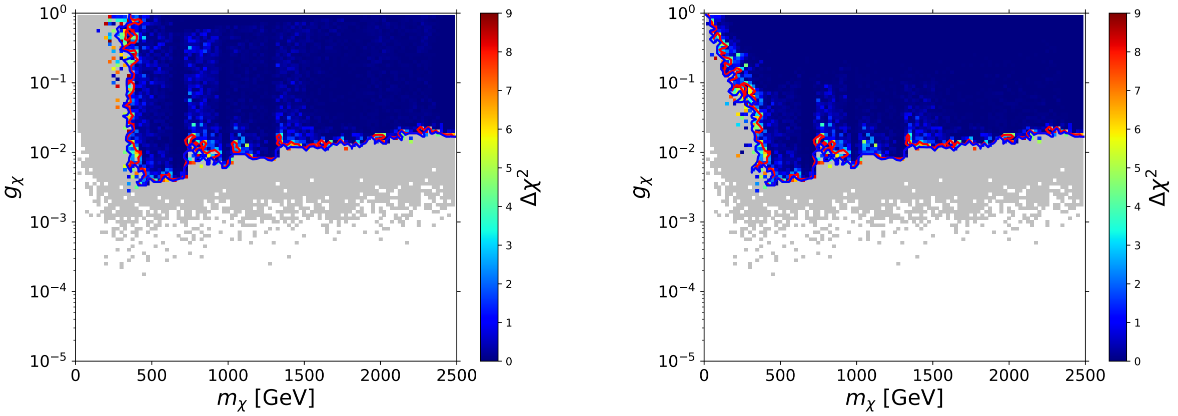

(c) $g_l < 0.1$

(d) $\Gamma_Y/m_Y < 0.1$

Figure 5.14: Comparison of the likelihood functions in the $(m_\chi,\, g_\chi)$ plane for different upper bounds on the lepton coupling g_l and the additional constraint $\Gamma_Y/m_Y < 0.1$. Top left: $g_l < 0.001$. Top right: $g_l < 0.01$. Bottom left: $g_l < 0.1$. Bottom right: $\Gamma_Y/m_Y < 0.1$. Note that the y-axis is shown on a logarithmic scale. All the plots are coloured according to the values of $\Delta\chi^2 = \chi^2 - \chi^2_{\text{min}}$, and the points for which $\Delta\chi^2 > 9$ are displayed in grey. The 1-σ and 2-σ regions are delineated by red and blue contours, respectively.

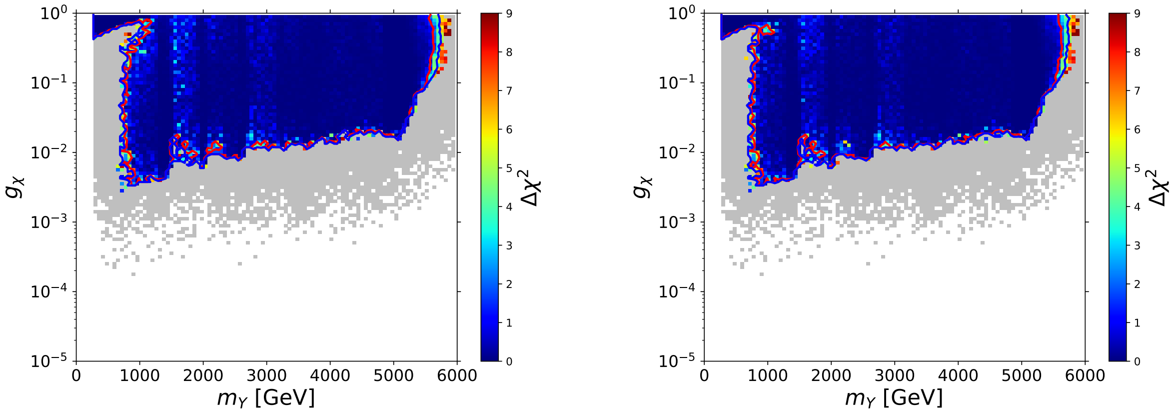

(a) $g_l < 0.001$ (b) $g_l < 0.01$

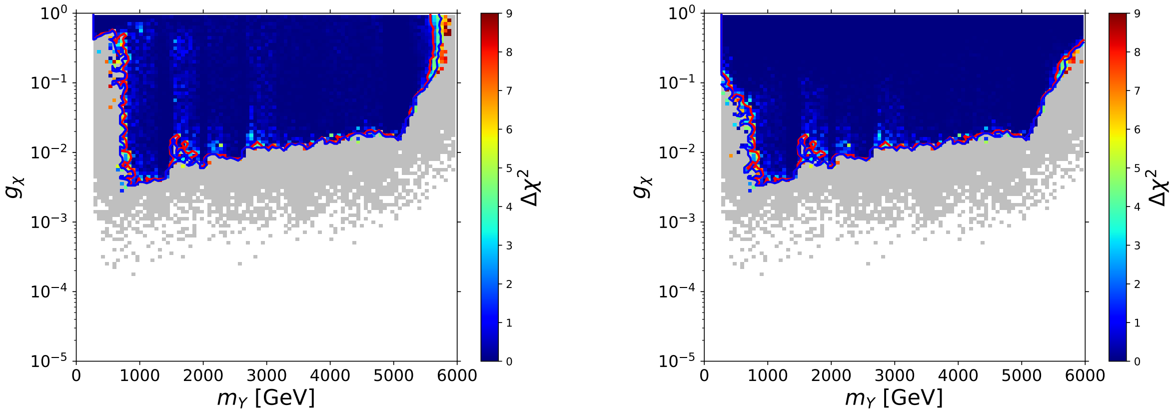

(c) $g_l < 0.1$ (d) $\Gamma_Y/m_Y < 0.1$

Figure 5.15: Comparison of the likelihood functions in the $(m_Y,\, g_\chi)$ plane for different upper bounds on the lepton coupling g_l and the additional constraint $\Gamma_Y/m_Y < 0.1$. Top left: $g_l < 0.001$. Top right: $g_l < 0.01$. Bottom left: $g_l < 0.1$. Bottom right: $\Gamma_Y/m_Y < 0.1$. Note that the y-axis is shown on a logarithmic scale. All the plots are coloured according to the values of $\Delta\chi^2 = \chi^2 - \chi^2_{\text{min}}$, and the points for which $\Delta\chi^2 > 9$ are displayed in grey. The 1-σ and 2-σ regions are delineated by red and blue contours, respectively.

Chapter 6

Conclusions and future work

Throughout this work, we have analysed a very general theoretical framework on the search for DM particles. In particular, we have performed a global analysis on a DMSM with a leptophilic spin-1 vector mediator, and we have included the latest experimental results as constraints on the model. Specifically, we have included the DM relic density constraint, the latest results from direct detection experiments and the three most accessible signatures at the LHC: monojet, dijet and dilepton. This work aims to understand which regions of our model's parameter space are compatible with the observations and which ones are excluded.

From the results obtained, we have analysed and tried to understand the new allowed regions that appear when g_l is non-zero, with respect to the ones seen in [21] for the leptophobic scenario. Moreover, we have compared the results obtained for different upper bounds on g_l to study the variations in the regions of the plane as we allow higher values of this coupling. The results have been projected onto various planes of parameter space:

$$(m_Y, m_\chi),\ \ (g_q, g_\chi),\ \ (m_\chi, g_q),\ \ (m_Y, g_q),\ \ (m_\chi, g_\chi)\ \text{and}\ (m_Y, g_\chi).$$

Starting with the (m_Y, m_χ) plane, we have first verified that when g_l tends to zero, we recover the results from the leptophobic scenario. Moreover, we have found new allowed regions that predict the correct value for the relic density when we allow the mediator coupling to leptons. We have also noted that the DM relic density is a strongly constraining observable since it is responsible for shaping the contours. In addition, the two possible dark matter annihilation mechanisms have been shown: annihilation via the t-channel and s-channel.

Considering figures 5.11, 5.12, 5.13, 5.14 and 5.15, we draw the following conclusions from a more general point of view. First, the significant lack of statistics when the cutoff on g_l is very restrictive, and the increase in the number of points as g_l is more allowed. This is probably because we are imposing such a restrictive cut on g_l that the number of sampled points is very low, so the program cannot find the minimum values of χ^2. As we increase the cutoff, more points are computed since it is easier to find such minimal values. Even though, for low values of g_χ, there is still a lack of statistics even if we fully allow g_l. The way to fix this issue is to perform a new dedicated sampling focusing on the subspace of low values of the couplings to recover all the missing points. This process has not been carried out in this work due to the lack of time, as the sampling might take several months. Therefore, we have been careful not to draw conclusions on the regions presented in this paper as excluded because they might not represent the full picture of the sampled parameter space.

In general terms, the DM relic density constraint seems to be the one that restricts the allowed regions and defines both lower and upper limits in the couplings, together with the effect of dijet constraints on g_q and m_Y.

We now give a perspective on the future work that remains to be done in this direction. In previous chapters, we have made some assumptions recommended by the LHCDMWG. However, these are only recommendations, which means that the counter-scenarios are not excluded, and it would be interesting to develop other simplified models to study them. Some examples are the following:

- Leptophilic axial-vector. The results for the vector and axial-vector interactions in a leptophobic scenario are published in [21]. In this work, we present the results for a spin-1 leptophilic mediator and a pure vector interaction. Therefore, the first possibility that comes to mind is to repeat our analysis in a leptophilic scenario for the axial-vector case. For example, in figures 3.2 and 3.3, we observed different results for the axial-vector interaction in both leptophilic and leptophobic scenarios with fixed couplings.

- Mixed vector and axial-vector couplings. For instance, we could consider axial-vector couplings to quarks and vector couplings to DM.

- Majorana fermion. Recall that we have assumed that our DM particle is a Dirac fermion (i.e. a fermion which is different from its antiparticle). All fermions in the SM are Dirac particles, except neutrinos, which we still do not know whether they belong to one group or the other. Hence, we could consider the opposite: a Majorana fermion, which is a fermion that is its own antiparticle.

- Spin-0 mediator. We could also choose a spin-0 mediator particle, like the Higgs boson. In this situation, the mediator would be a scalar or pseudoscalar particle, and it would probably add other interesting signatures to the model.

- Quark flavour violation. In section 2.2, we mentioned that we do not mix flavours at the interactions between the mediator and the SM particles (for both leptons and quarks). However, according to the SM, quarks are allowed to swap their flavours through the weak force. For instance, an up quark can turn into a down quark when it interacts with the W^- boson [48]. Therefore, we could implement new interactions where the flavours of the quarks change when interacting with the mediator.

These are some ideas that may arise from what has been described in this work, and MasterCode seems to be a suitable tool for performing these analyses. Undoubtedly, there are many more options, and it is important to study them further to cover more possible scenarios. The more information we can obtain from them, the better our understanding of these simplified models, which are key for analysing more complex models involving new parameters.

We should keep in mind that DMSM are not thought to be a final theory but an effective way to represent new physics and understand how DM connects to the SM. In fact, the interactions we have described in this work are an interpretation of more complex processes. Moreover, the constraints we have implemented also come from various directions, so it is complicated to understand which one(s) is responsible for which feature. Since so much is still unknown about DM, from these results, we could better understand what is still a physical option and use this knowledge for guidance on where to concentrate future searches. We started this work by asking: *"If ordinary matter only accounts for 5% of the composition of the Universe, then what is the rest made of?"* Hopefully, one day, we are able to give an answer to this question.

Bibliography

[1] *ATLAS experiment.* URL: `https://atlas.cern`.

[2] *CMS experiment.* URL: `https://cms.cern`.

[3] *LUX DM experiment.* URL: `http://luxdarkmatter.org`.

[4] *PandaX DM experiment.* URL: `https://pandax.sjtu.edu.cn`.

[5] *XENON experiment.* URL: `http://www.xenon1t.org`.

[6] Aghanim N. et al. [Planck Collaboration]. "Planck 2013 results. XVI. Cosmological parameters". In: *Astronomy and Astrophysics* 571 (2014), A16. DOI: `10.1051/0004-6361/201321591`. arXiv: `1303.5076 [astro-ph]`.

[7] Hooper D. Bertone G. and Silk J. "Dark Matter: Evidence, Candidates and Constraints". In: *Physics Reports* 405 (2005), pp. 5–6. DOI: `https://doi.org/10.1016/j.physrep.2004.08.031`. arXiv: `hep-ph/0404175`.

[8] Raffelt G. "Dark Matter: Motivation, Candidates and Searches". In: *The 1997 European School of High-Energy Physics* (1997), pp. 235–278. arXiv: `hep-ph/9712538`.

[9] John I. *Summarising constraints on dark matter at the Large Hadron Collider.* 2017. URL: `http://lup.lub.lu.se/student-papers/record/8903100`.

[10] Trevisani N. "Search for Dark Matter produced in association with a Higgs boson in the W^+W^- fully leptonic decay channel in pp collisions at $\sqrt{s} = 13\text{TeV}$ at the LHC with the CMS detector." 2019. URL: `http://cds.cern.ch/record/2692363`.

[11] P. S. Bhupal Dev, Anupam Mazumdar, and Saleh Qutub. "Constraining non-thermal and thermal properties of Dark Matter". In: *Frontiers in Physics* 2 (2014). DOI: `10.3389/fphy.2014.00026`.

[12] Amidei D. Aguilar-Arevalo A. et al. *The DAMIC dark matter experiment.* 2015. DOI: `10.22323/1.236.1221`. arXiv: `1510.02126 [physics.ins-det]`.

[13] Brown University Particle Astrophysics Group. *Brown Particle Astrophysics webpage.* URL: `https://particleastro.brown.edu/dark-matter`.

[14] Ellis J. "TikZ-Feynman: Feynman diagrams with TikZ". In: *Computer Physics Communications* 210 (2016). DOI: `10.1016/j.cpc.2016.08.019`. arXiv: `1601.05437 [hep-ph]`.

[15] Akchurin N. Abercrombie D. et al. “Dark Matter benchmark models for early LHC Run-2 Searches: Report of the ATLAS/CMS Dark Matter Forum”. In: *Physics of the dark universe* 27 (2020). DOI: `10.1016/j.dark.2019.100371`. arXiv: `1507.00966 [hep-ex]`.

[16] Araujo H. Abdallah J. et al. “Simplified models for dark matter searches at the LHC”. In: *Physics of the dark universe* 9-10 (2015), pp. 8–23. DOI: `10.1016/j.dark.2015.08.001`. arXiv: `1506.03116 [hep-ex]`.

[17] Buchmueller O. Boveia A. et al. *Recommendations on presenting LHC searches for missing transverse energy signals using simplified s-channel models of dark matter.* 2016. arXiv: `1603.04156 [hep-ex]`.

[18] *The SM of particle physics.* URL: `https://upload.wikimedia.org/wikipedia/commons/0/00/Standard_Model_of_Elementary_Particles.svg`.

[19] Thomson M. *Modern Particle Physics.* Cambridge University Press, 2013.

[20] Dolan M.J. Buchmueller O. et al. “Characterising dark matter searches at colliders and direct detection experiments: vector mediators”. In: *Journal of High Energy Physics* 2015.1 (2015). DOI: `10.1007/jhep01(2015)037`. arXiv: `1407.8257 [hep-ph]`.

[21] Bagnaschi E. Heinemeyer S. et al. “Global analysis of dark matter simplified models with leptophobic spin-one mediators using MasterCode”. In: *European Physical Journal* 79 (2019), pp. 235–278. DOI: `10.1140/epjc/s10052-019-7382-3`. arXiv: `1905.00892 [hep-ph]`.

[22] Fairbairn M. Ellis J. and Tunney P. *Phenomenological Constraints on Anomaly-Free Dark Matter Models.* 2018. arXiv: `1807.02503 [hep-ph]`.

[23] Boudjema F. Bélanger G. et al. “micrOMEGAs3: A program for calculating dark matter”. In: *Computer Physics Communications* 185.3 (2014), pp. 960–985. DOI: `10.1016/j.cpc.2013.10.016`. arXiv: `1305.0237 [hep-ph]`.

[24] Alsum S. et al. [LUX Collaboration]. “Results from a Search for Dark Matter in the Complete LUX Exposure”. In: *Physical Review Letters* 118 (2017). DOI: `10.1103/physrevlett.118.021303`. arXiv: `1608.07648 [astro-ph]`.

[25] Cui X. et al. [Panda Collaboration]. “Dark Matter Results from 54-Ton-Day Exposure of PandaX-II Experiment”. In: *Physical Review Letters* 119.18 (2017). DOI: `10.1103/physrevlett.119.181302`. arXiv: `1708.06917 [astro-ph]`.

[26] Aprile E. et al. [XENON Collaboration]. “Dark Matter Search Results from a One Ton-Year Exposure of XENON1T”. In: *Physical Review Letters* 121.11 (2018). DOI: `10.1103/physrevlett.121.111302`. arXiv: `1805.12562 [astro-ph]`.

[27] [ATLAS Collaboration] CERN. *Search for New Phenomena in Dijet Events using 139 fb^1 of pp collisions at $\sqrt{s}$ = 13TeV collected with the ATLAS Detector.* 2019. URL: `http://cds.cern.ch/record/2668385`.

[28] Tumasyan A. Sirunyan A. M. et al. “Search for new physics in final states with an energetic jet or a hadronically decaying W or Z boson and transverse momentum imbalance at s=$\sqrt{13}$ TeV”.

In: *Physical Review D* 97.9 (2018). DOI: `10.1103/physrevd.97.092005`. arXiv: `1712.02345 [hep-ex]`.

[29] Tumasyan A. Sirunyan A. M. et al. “Search for narrow and broad dijet resonances in proton-proton collisions at $\sqrt{s} = 13\text{TeV}$ and constraints on dark matter mediators and other new particles”. In: *Journal of High Energy Physics* 2018.8 (2018). DOI: `10.1007/jhep08(2018)130`. URL: `http://dx.doi.org/10.1007/JHEP08(2018)130`.

[30] [ATLAS Collaboration]. “Search for new light resonances decaying to jet pairs and produced in association with a photon or a jet in proton-proton collisions at $\sqrt{s} = 13$ TeV with the ATLAS detector”. In: (2016). URL: `http://cds.cern.ch/record/2206221`.

[31] ATLAS Collaboration. “Search for light dijet resonances with the ATLAS detector using a Trigger-Level Analysis in LHC pp collisions at $\sqrt{s} = 13$ TeV”. In: (2016). URL: `https://cds.cern.ch/record/2161135`.

[32] Tumasyan A. Sirunyan A. M. et al. “Search for low mass vector resonances decaying into quark-antiquark pairs in proton-proton collisions at $\sqrt{s} = 13$ TeV”. In: 2018.1 (2018). DOI: `10.1007/jhep01(2018)097`. URL: `http://dx.doi.org/10.1007/JHEP01(2018)097`.

[33] Aad G. Aaboud M. et al. “Search for new phenomena in dijet events using 37fb1 of pp collision data collected at $\sqrt{s} = 13$ TeV with the ATLAS detector”. In: 96.5 (2017). DOI: `10.1103/physrevd.96.052004`. URL: `http://dx.doi.org/10.1103/PhysRevD.96.052004`.

[34] Aad G. Aaboud M. et al. “Search for high-mass dilepton resonances using 139 fb1 of pp collision data collected at s=13 TeV with the ATLAS detector”. In: *Physics Letters B* 796 (2019), pp. 68–87. DOI: `10.1016/j.physletb.2019.07.016`.

[35] Chala M. Kahlhoefer F. et al. “Constraining dark sectors with monojets and dijets”. In: *Journal of High Energy Physics* 7 (2015). DOI: `10.1007/JHEP07(2015)089`. arXiv: `1503.05916 [hep-ph]`.

[36] *The MasterCode project.* URL: `http://mastercode.web.cern.ch`.

[37] Costa J.C. “Global analyses of BSM theories using LHC Run 2”. In: *Physics PhD theses, Imperial College London* (2019). DOI: `10.25560/81763`.

[38] Sakurai K. Papucci M. et al. “Fastlim: a fast LHC limit calculator”. In: *The European Physical Journal* 74.11 (2014). DOI: `10.1140/epjc/s10052-014-3163-1`.

[39] Duhr C. Alwall J. et al. “Computing decay rates for new physics theories with Feynman Rules and MadGraph5aMC@NLO”. In: *Computer Physics Communications* 197 (2015), pp. 312–323. DOI: `10.1016/j.cpc.2015.08.031`. arXiv: `1402.1178 [hep-ph]`.

[40] Hobson M. P. Feroz F. and Bridges M. “MultiNest: an efficient and robust Bayesian inference tool for cosmology and particle physics”. In: *Monthly Notices of the Royal Astronomical Society* 398.4 (2009), pp. 1601–1614. DOI: `10.1111/j.1365-2966.2009.14548.x`. arXiv: `0809.3437 [astro-ph]`.

[41] *SQLite.* URL: `https://www.sqlite.org`.

[42] *The VIM Editor*. URL: `https://www.vim.org`.

[43] *Matplotlib: Visualization with Python*. URL: `https://matplotlib.org`.

[44] *Oracle VM VirtualBox*. URL: `https://www.virtualbox.org`.

[45] *Docker*. URL: `https://www.docker.com`.

[46] *Singularity*. URL: `https://singularity.hpcng.org`.

[47] *HTCondor*. URL: `https://research.cs.wisc.edu/htcondor`.

[48] CMS Collaboration. *A close and complicated relationship: the top quark and the W boson intertwine*. URL: `https://cms.cern/news/close-and-complicated-relationship-top-quark-and-w-boson-intertwine`.